



PlanetWRF: A general purpose, local to global numerical model for planetary atmospheric and climate dynamics

Mark I. Richardson,¹ Anthony D. Toigo,^{2,3} and Claire E. Newman¹

Received 8 September 2006; revised 15 March 2007; accepted 7 May 2007; published 14 September 2007.

[1] A new planetary atmospheric numerical model, “planetWRF,” has been developed by modifying the Weather Research and Forecasting (WRF) model. The model has generalized map projection, multiscale, and nesting capabilities, blurring the distinction between global and mesoscale models and enabling investigation of coupling between processes on all scales, including global. The model can also be run in one, two, or three dimensions. The conversion of the dynamical core for global application by altering the map projection grid and the boundary conditions as well as conversion of the physics parameterizations and constants for planetary application are described. Validation of the global dynamical core through use of standard forcing scenarios is presented. Example results from a series of simulations for Mars, Titan, and Venus are shown to demonstrate that the model performs well for a variety of planets and operating modes (microscale, mesoscale, and global scale).

Citation: Richardson, M. I., A. D. Toigo, and C. E. Newman (2007), PlanetWRF: A general purpose, local to global numerical model for planetary atmospheric and climate dynamics, *J. Geophys. Res.*, 112, E09001, doi:10.1029/2006JE002825.

1. Introduction

[2] We have developed a new model for numerical simulation of planetary atmospheres and climate systems. The model has many advantages over previous models used by our research group [e.g., Richardson and Wilson, 2002; Toigo and Richardson, 2003], but differs significantly by virtue of its generalized map projection, multiscale and nesting (“zooming” in to higher resolution over part of the domain) capabilities, obviating the distinction between global and mesoscale models. As such, the model enables investigation of coupling between processes on a variety of scales, including global. Such interscale interactions appear to be important, for example, in the case of Martian dust storm expansion from local to global extent [e.g., Kahn *et al.*, 1992; Zurek *et al.*, 1992]. In this case, of likely importance are intricate feedbacks between the local scale meteorology, which controls initial storm development and dust opacity rise (increasing radiative heating of the atmosphere), and the global-scale circulation, which both modifies the local-scale meteorology and is responsible for regional and global spread of lifted dust. Analogous scale feedbacks are of likely importance for cloud formation in a variety of atmospheres, including those of Titan and the Earth. Indeed, the coupling of higher-resolution domains with terrestrial global models to study (or in some cases,

rather to parameterize) the influence of mesoscale cloud formation processes has been ongoing for some time [e.g., Khairoutdinov *et al.*, 2005]. The generalized computational grid also allows the model to be configured in one-, two-, or three-dimensional mode at runtime, allowing the impact of dimensionality and validity of modeled physical processes to be tested without the complication of switching model dynamical cores (e.g., Lagrangian versus Eulerian) or numerical solvers (e.g., leapfrog versus Runge-Kutta).

[3] Global numerical models integrating the primitive equations of atmospheric motion have been applied to a variety of planetary atmospheres since the 1960s [Leovy and Mintz, 1969], not long after their introduction into terrestrial atmospheric science. Arguably the most extensive nonterrestrial application has been to the Martian atmosphere, which until the mid-1990s was almost exclusively undertaken by the NASA Ames General Circulation Model (GCM) group [Pollack *et al.*, 1981, 1990, 1993; Haberle *et al.*, 1993b, 1999, 2003]. More recently, the population of Martian global models has bloomed, including the Geophysical Fluid Dynamics Laboratory (GFDL) Mars model [Wilson and Hamilton, 1996] (based on the GFDL Skyhi model), the Oxford-LMD (Laboratoire de Météorologie Dynamique) Mars model (two dynamical cores with shared parameterizations of sub-grid-scale physical processes) [Forget *et al.*, 1999; Lewis *et al.*, 1999], models based at York University in Canada [Moudden and McConnell, 2005], at Japanese universities [e.g., Takahashi *et al.*, 2003; Kuroda *et al.*, 2005], and at the Max Planck Institute for Solar System Research in Germany [Hartogh *et al.*, 2005]. Titan’s atmosphere has been the target of global modeling efforts since the mid-1990s, with recent renewed interest and greater emphasis due to the Cassini-Huygens mission. The most developed of these Titan GCMs are the

¹Division of Geological and Planetary Sciences, California Institute of Technology, Pasadena, California, USA.

²Graduate School of Science and Technology, Kobe University, Kobe, Japan.

³Now at Department of Astronomy, Cornell University, Ithaca, New York, USA.

LMD [e.g., Hourdin et al., 1995; Lebonnois et al., 2003; Rannou et al., 2004; Luz et al., 2003] and Cologne University models [e.g., Tokano et al., 1999; Tokano and Neubauer, 2002; Tokano, 2005]. Venus's atmosphere has also been modeled using modified versions of the CCSR/NIES (Center for Climate System Research, University of Tokyo; National Institute for Environmental Studies, Japan) GCM [Yamamoto and Takahashi, 2003a, 2003b, 2004] and the United Kingdom Meteorological Office (UKMO) Unified Model (UM) [Lee et al., 2005]. In addition, the atmospheres of the giant planets have been the main focus of the only GCM custom-designed for planetary modeling, the Explicit Planetary Isentropic Coordinate (EPIC) model [Dowling et al., 1998], and the UM has also been applied to Jupiter [Yamazaki et al., 2004].

[4] Limited area (or mesoscale/microscale) models have been used for weather forecasting applications on Earth since the 1970s, but only recently have such models been used for planetary atmospheres, the main impediment being the lack of surface data to constrain the lower boundary for the latter case. Mesoscale models have been applied to Mars for several years now, often being used to interpret landed spacecraft data and examine meteorological systems on substantially subglobal scales [Rafkin et al., 2001; Toigo and Richardson, 2002; Tyler et al., 2002], and Titan mesoscale models are becoming increasingly common [e.g., Hueso and Sánchez-Lavega, 2006]. Large eddy simulation, or LES, modeling, allows simulation of dynamics on scales down to a few meters in order to explicitly simulate the boundary layer [Toigo et al., 2003; Michaels and Rafkin, 2004]. The lateral boundary conditions of all these limited area models must either be forced from an archive of global model results, or be set as periodic in idealized simulations.

[5] Some models have begun to push at the distinction between global and mesoscale modeling. One approach is to “zoom” a global domain by distorting the map projection, causing clustering of grid points in a specified location [e.g., Fox-Rabinovitz et al., 2000]. The LMD, York University and NASA Ames planetary models discussed above are capable of this numerical contortion. This type of zooming is useful, but restricted insofar as the placement, number, and extent of high-resolution patches within the domain are concerned (for example, only two patches at most can be introduced). While such zooming is a useful intermediate solution to examination of multiscale processes, a fully generalized computational grid is desirable. This can be accomplished in at least two ways: by switching to a grid of nearly equally spaced polygonal grid boxes; or, by using the nesting machinery built into mesoscale models, and relaxing the map projection to allow for global (single or tiled domain) extent. The former solution is arguably more elegant, however, the latter would allow greater compatibility with previous models (a traditional GCM can be emulated), and greater flexibility in terms of grid configuration. We have chosen to follow the latter path.

[6] In this paper, we describe a global, planetary model based on the Weather Research and Forecasting (WRF) model, henceforth termed the “planetWRF” model. In section 2, we briefly review the original WRF model, which is described in much greater detail in a National Center for Atmospheric Research (NCAR) Technical Note [Skamarock et al., 2005] and user's guide (<http://www.wrf-model.org>).

In section 3, we go on to describe the two main modifications to WRF required to develop the planetWRF model. The first makes the model global by generalizing the computational grid to allow for nonconformal map projections (specifically simple cylindrical), then adding polar boundary conditions and filtering. The second makes the model a more general planetary atmospheric model by modifying both how physical constants are specified and the model's “clocks and calendar” routines, at which point specific atmospheres can be addressed by adding appropriate parameterizations of physical processes (e.g., radiative transfer schemes). In section 4, we examine the validity of the global (but not yet planetary) WRF dynamical core using a number of simplified and idealized simulations. In section 5, we illustrate planetary application of the non-global (and thus more nearly original) WRF model for a large eddy simulation and a regional mesoscale simulation, both for Mars. The validity of the dynamical core in this configuration has been demonstrated extensively for the Earth as a part of the NCAR development effort, and thus we will not do so here. In section 6, we proceed to show full global and planetary application of the model for Mars, Titan and Venus. Our main intention here is to demonstrate the model's capabilities and versatility, rather than present detailed validation by comparison with observations; this is deferred to upcoming papers focusing on the specific planetary applications. Finally, a summary is provided in section 7.

2. Weather Research and Forecasting Model

[7] The Weather Research and Forecasting (WRF) model is a co-development of NCAR, the National Oceanographic and Atmospheric Administration (NOAA), the US Department of Defense, and various universities [Michalakes et al., 2004; Skamarock et al., 2005]. WRF is a state of the art mesoscale model used for both research and operational forecasting, this dual purpose being a key design feature intended to speed the application of new scientific and modeling developments into practical forecasting usage. The model has been constructed to be highly modular, such that different physical packages and dynamical cores can be used. In this study, we only consider WRF as implemented using the “Eulerian mass” dynamical core, and all further description relates to this version of the WRF model, known within the WRF community as the Advanced Research WRF (WRF-ARW). The code is written primarily in Fortran 90, and has been designed to run on a variety of single processor, and distributed- and shared-memory parallel processor computers. The model, while being written completely from scratch, is intended to supersede the previous NCAR-managed Mesoscale Model Version 5 (MM5), and inherits much knowledge gained through more than 20 years' use of that model, including improvements in dynamical cores and physical parameterizations.

[8] Although originally designed as a mesoscale model, the WRF dynamical core is quite general and appropriate for treatment of fluid flow on scales from meters to thousands of kilometers. The core integrates the fully compressible, Euler equations in flux form. An option allows the core equations to be solved fully or using the hydrostatic approximation. The full three-dimensional Coriolis and curvature effects are treated. WRF is a grid point

model based around a horizontal Arakawa C-grid [Arakawa and Lamb, 1977]. In the vertical, the terrain-following hydrostatic pressure (“eta”) coordinate is used [Laprise, 1992], defined by the hydrostatic component of the local pressure, the surface pressure, and the fixed model top pressure (for a simulation using the hydrostatic approximation, this is exactly the standard “sigma” coordinate [e.g., Jacobson, 1999]). The key prognostic variables are the horizontal (and in nonhydrostatic mode, the vertical) winds, potential temperature, column-integrated mass per unit area, and geopotential. In both the horizontal and vertical, for vector (momentum) and scalar variables, the code allows a run-time choice of 2nd to 6th order advection. Time integration uses a leapfrog or 2nd or 3rd order Runge-Kutta scheme (again, selected by the user), with a sub-time-step treatment of acoustic and fast gravity wave modes [Wicker and Skamarock, 2002; Skamarock et al., 2005]. Only the 3rd order Runge-Kutta method is stable for all choices of grid discretization and spatial differencing. Sub-grid-scale diffusion can be calculated on the model (eta) surfaces or in physical (x, y, z) space, with the diffusion coefficients being defined (1) as globally constant, (2) using a 1.5 order turbulent kinetic energy closure scheme, or (3) using two- or three-dimensional versions of the 1st order Smagorinsky deformation scheme [Smagorinsky, 1963]. When a planetary boundary layer (PBL) parameterization is specified, the vertical diffusion is handled by that scheme instead of the dynamical core diffusion scheme. Physical process models (physical parameterizations) can be called from the WRF solver within the acoustic time stepping, within the Runge-Kutta time stepping, or at the end of the time loop using additive time splitting. Issues of stability and conservation provide the criteria for location of the calls.

[9] WRF has been designed to be flexible from the perspective of boundary condition definition and map projection. Run-time options to implement periodic, symmetric, open, and forced boundary conditions exist. The last of these is critical to implementation of a traditional mesoscale model (where the limited area model boundaries are forced by data or output from another model) and nested modeling applications. WRF includes the infrastructure necessary for the run-time definition of multiple parallel and downward levels of nesting, with one- or two-way interactivity and the option of nest motion within the mother domain. Map projection is generalized (to a limited degree; see the next section) by the use of map scale factors for each grid point that define the computational-to-physical space projection of the domain. The WRF model is designed to run in the three basic conformal map projections (Mercator, Lambert conformal, and polar stereographic), as the integrated equations will be the same, while only the value of map scale factor will change for each projection.

3. Modifications of WRF for Global and Planetary Application

[10] Our interest in WRF stems from our desire to implement a more capable mesoscale/microscale model for Mars than our existing NCAR MM5-based model [Toigo and Richardson, 2003], to eliminate numerical model-to-model differences between our global and limited area models, and to develop a single framework within which

to study local-to-global coupled dynamical processes. This desire to build a flexible and general workhorse for planetary atmospheric/climate system modeling places tough requirements on the base model chosen for planetary modification, yet development of a new model from scratch would not have taken advantage of the considerable investment in terrestrial modeling made by various organizations. While WRF has many of the required attributes for a truly comprehensive modeling system, it had two major drawbacks for our purposes: it was not configured such that a fully global domain could be simulated, and was written to be exclusively applicable to the Earth. Our development work was thus focused on making the choice of map projection more general (to include both conformal and nonconformal map projections), on including specific boundary conditions and filtering necessary to allow the model to be run as a traditional, C-grid GCM, and on generalizing the specification of planetary constants and timing conventions. These modifications are described here in sections 3.1, 3.2, and 3.3, respectively. We also describe in section 3.4 the additional parameterizations of physical processes required for Mars and Titan work.

3.1. Nonconformal Grid Modification

[11] WRF was built to use only conformal map projections, meaning that the map scale factors (which relate map projection distance to physical distance) are independent of direction. This assumption means that for each point on the grid, only a single map scale factor need be defined. The use of only a single map scale factor for each grid point simplified the equations and allowed some cancellation of terms. The cost of this simplification was that (by definition) only conformal map projections could be used: polar stereographic, Lambert conformal, Mercator, and simplified/idealized square grid boxes. This set of choices provides great flexibility for mesoscale and microscale modeling, but eliminates the possibility of using the model as a fully global single domain.

[12] The simple cylindrical map projection that is used for most grid point GCMs is a nonconformal projection. Indeed, any grid that seeks to represent the full globe on a single, rectangular domain must be nonconformal (for example, consider trying to make a global Mercator domain: as the pole is approached, the zonal grid separation tends to zero, forcing the meridional separation to tend to zero, such that the pole cannot be reached). Generalization of the model so that nonconformal map projections can be used requires the equations to be rewritten with the full, separate x- and y-directional map scale factor components. A full derivation of the equations used in the global WRF model is provided in Appendix A. Although implemented primarily to allow WRF to run with a traditional latitude-longitude (simple cylindrical) GCM map projection, the modifications allow any generalized map projection to be used, including rotated pole (transverse projection, see section 6.1 and Appendix C) and stretched/zoomed grids [e.g., Fox-Rabinovitz et al., 2000].

3.2. Polar Boundaries and Filtering

[13] Using a simple cylindrical map projection, a grid point domain can be defined that uniformly covers the globe in latitude-longitude space. In the east-west direction, the

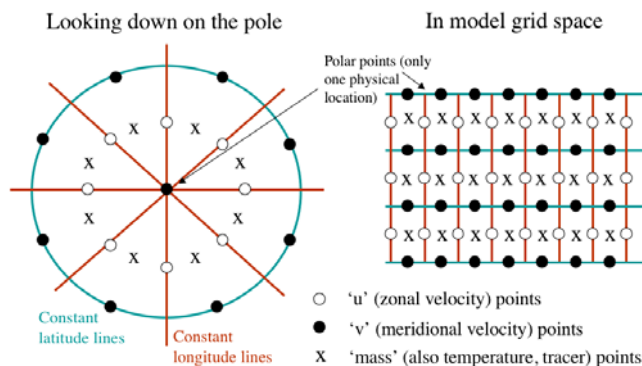


Figure 1. The global WRF grid, both (left) looking down on the pole (“real space”) and (right) in a C-grid cylindrical projection (grid points equally spaced in longitude and latitude, with horizontally staggered u , v , and mass points). All of the v points occurring at a pole actually correspond to only one physical location.

appropriate boundary condition is periodic (allowing flow across the border and onto the opposite side of the domain), which was already an option in the original version of WRF. In the north-south direction, a “polar” boundary condition is needed. We have followed the convention for C-grid models used, for example, by the GSFC Aries model [Suarez and Takacs, 1993; Fox-Rabinovitz et al., 1997]. We take the polar point to be a C-grid v -stagger point (see Figure 1), and have chosen the simplest possible polar boundary condition by setting the value of the meridional velocity (“ v ”) constantly equal to zero. In the near future this will be replaced by a more sophisticated implementation. Flux and gradient calculations across the pole are not allowed. It is important to note that this does not preclude advection of material across the pole: “over the pole” advection is instead accomplished by zonal transport within the most poleward zone (see section 4.1).

[14] The convergence of the zonal grid points approaching the pole can present another well-known problem. The physical distance for zonal advection of information decreases rapidly to zero at the pole. The most poleward zonal grid points are located half a full grid spacing from the pole, and since these are the least separated of all grid points in the domain, they will determine the model time step needed to avoid instability in the horizontal direction (the Courant-Friedrichs-Lewy, or CFL, criteria [e.g., Kalnay, 2002]). If a time step more appropriate to the tropical latitudes (i.e., much longer) is to be used in the model, then some approach to damping instability in the high latitudes must be applied. We have implemented Fourier filtering of the higher-frequency components of state variables in the global-capable version of WRF. After some experimentation we have settled on an approach wherein all grid points poleward of 60° are filtered, with the cutoff frequency being a function of the cosine of latitude (see Appendix B). The column mass, horizontal winds, temperature and tracers (moisture, aerosols, chemicals, etc.) are filtered. This arrangement was found to yield the greatest stability.

3.3. Generalized Planetary Parameters and Timing Conventions

[15] WRF utilizes a centralized module to hold commonly needed planetary and atmospheric constants (e.g., gravity

and ideal gas constants). We have taken advantage of this by additionally centralizing such variables as the orbital parameters, the relationship between SI seconds and model seconds (the latter being defined as $1/86400$ of a planetary rotational period, see the next paragraph), and the reference pressure. We have made the selection of a set of consistent planetary parameters a compilation-time option. The collocation of all model constants in one module makes setting them up for any arbitrary planet very straightforward.

[16] The model assumes that one day is made up of 24 hours, each of which is composed of 60 min, in turn made up of 60 s. The model time step is externally defined in terms of these planetary time units, thus there is always an integer number of time steps per day. However, the dynamics and physics routines are still integrated in MKS (SI) units, with the conversion from model-to-SI time made before calculating tendencies and physical quantities.

[17] The original WRF version uses the standard day-month-year calendar format. This convention is used to drive the solar radiation routines and to label model output. WRF uses routines from the standardized Earth System Modeling Framework (ESMF) (<http://www.esmf.ucar.edu>). We have converted versions of these routines to drive the model with user-specified orbital elements using the planetocentric solar longitude (L_s) date system (with $L_s = 0^\circ$ corresponding to northern hemisphere spring equinox and $L_s = 90^\circ$ to northern hemisphere summer solstice, etc.).

3.4. Parameterizations of Sub-Grid-Scale Physical Processes

[18] For Mars, physical parameterization routines have been added to WRF to treat radiative transfer in a dusty, CO_2 atmosphere (section 3.4.1), and to account for the seasonal condensation/sublimation of CO_2 ice to/from the polar caps (where temperatures fall below the condensation point in autumn and winter; section 3.4.2). For Titan, we have added an updated version of the radiative transfer scheme described by McKay et al. [1989] (section 3.4.3). Simple surface drag and radiative relaxation schemes, similar to the Held and Suarez [1994] forcing we used to validate the global dynamical core (described in section 4.2), have been used to treat the Venusian atmosphere (results are shown in section 6.3), though more sophisticated radiative transfer parameterizations will be added in the

near future. For all planets, we use WRF's existing horizontal and vertical diffusion parameterization schemes, as the physics of diffusion will remain the same with only the diffusivities varying. It should be noted that WRF has been designed to readily and rapidly accommodate new physics routines, thus planetWRF is neither limited to nor defined by the physics routines current in the model at the time of writing.

3.4.1. Radiative Transfer on Mars

[19] In the Martian version of the planetWRF model ("MarsWRF"), the radiative transfer scheme accounts for (1) absorption and emission of thermal infrared radiation in the broad CO₂ 15 μm band, (2) absorption of incoming solar radiation in the near-infrared CO₂ bands (significant above 50 km or so), (3) absorption and scattering of incoming solar radiation by dust, and (4) scattering of infrared radiation outside the 15 μm band by dust. While we have implemented several radiative transfer schemes, the one used in Mars simulations described in this paper is almost exactly that used in the Oxford-LMD Mars GCM (described by *Forget et al.* [1999]) in order to enable direct comparisons with the results of that model and the associated Mars Climate Database (MCD) [*Lewis et al.*, 1999]. The main change to the radiative transfer scheme relative to that described by *Forget et al.* [1999] is the incorporation of additional non-LTE (local thermodynamic equilibrium) cooling above approximately 60 km. This modification is based on tabulated cooling rates calculated by *Lopez-Valverde et al.* [1998].

[20] The model accounts for spatial, diurnal and seasonal changes in the solar forcing, and also includes various means of calculating the dust opacity distribution (both prescribed and interactive). In these simulations, a prescribed, time-varying spatial distribution of atmospheric dust has been used. This formulation is based on the "MGS scenario" developed for the MCD [*Lewis et al.*, 1999] to reproduce atmospheric temperatures during the first full year of MGS observations (thus, for example, our results during the dust storm season in particular are best compared with observations from this year, as shown by *Smith et al.* [2001]). As yet no model has been able to fully reproduce the observed dust cycle with active dust transport, i.e., with parameterized dust lifting, advection by model winds, and sedimentation, allowing the dust distribution and atmospheric state to evolve in a self-consistent manner [see, e.g., *Newman et al.*, 2002a, 2002b; *Basu et al.*, 2004; *Kahre et al.*, 2005, 2006]. Therefore here we only show results from simulations employing prescribed dust opacity.

3.4.2. CO₂ Condensation-Sublimation Flow on Mars

[21] Mars is unusual in that the dominant atmospheric component (CO₂, at approximately 95%) can condense/sublime in the atmosphere and at the surface. We parameterize this at each time step by calculating the surface heat balance. Any excess cooling below the condensation point temperature is ascribed to CO₂ condensation, while any heating excess predicted when CO₂ ice is on the surface is ascribed to sublimation. Similar considerations apply within the atmosphere, with any condensed CO₂ being immediately precipitated to the surface. Finally, we update the column mass (hence total atmospheric pressure at the surface) to account for gains to and losses from the atmosphere (in the

nonhydrostatic model, the mass is added to or removed from the lowest model layer). Because the atmospheric pressure changes due to this parameterization, we must also adjust any tracer mass mixing ratios, q , accordingly to avoid introducing spurious sinks and sources. Since the mass mixing ratio depends on the mass of air, even if the quantity (volume or mass) of aerosols remains the same, the ratio will change due to the change in column mass. This approach has been standard in Martian GCMs for many years. More detailed microphysics of CO₂ ice, especially in the atmosphere, is under study but not yet operationally implemented.

3.4.3. Radiative Transfer on Titan

[22] For Titan, an updated version of the scheme described by *McKay et al.* [1989] is currently used. At solar (visible and near-infrared) wavelengths, the scheme includes absorption by gaseous methane, Rayleigh scattering, and absorption and scattering by haze particles. Haze physical properties are found at each time step by means of a relatively simple model, which assumes that small haze particles are produced at a constant rate in the upper stratosphere then coagulate as they fall under gravity. The production rate and electrostatic charging factor are the model inputs, with the number and size of haze particles in each model layer being the steady state solution. In the infrared, the scheme takes account of collision-induced gaseous absorption by primarily N₂, CH₄ and H₂ (dominating in the lower atmosphere), and emission by C₂H₂ and C₂H₆ molecules and haze (dominating in the stratosphere). The sources are combined to give layer-averaged values of extinction, single scattering albedo and asymmetry factor, and input to a two-stream matrix solver (that of *Toon et al.* [1989]) to produce separate solar and infrared fluxes in each layer and thus net heating rates. The model accounts for spatial, diurnal, and seasonal changes in the solar forcing.

3.4.4. Diffusion

[23] Horizontal diffusion is generally unmodified in planetary WRF applications. The diffusion tendencies are calculated from the resolved wind field using diffusion coefficients calculated either (1) following the 2-D or 3-D Smagorinsky deformation approach [*Smagorinsky*, 1963], (2) using a function of the total of the local turbulent kinetic energy, or (3) using specified values. The choice of diffusion coefficient approach is made at runtime. For the global and mesoscale runs described here, the diffusivity is determined using the 2-D Smagorinsky approach, i.e., from the deformation of the local wind field. The LES uses the 3-D Smagorinsky scheme.

[24] Vertical diffusion can be handled either by using constant, specified vertical diffusion coefficients, or by using planetary boundary layer (PBL) parameterization schemes. PBL schemes are meant to parameterize vertically subgrid heating-induced and mechanically induced turbulence. Again the choice of how to deal with vertical diffusion is made at runtime. We typically choose to use one of WRF's existing PBL schemes, the MRF-PBL (Medium Range Forecast model PBL) parameterization, except when we attempt to explicitly model the atmospheric turbulence, as with large eddy simulations. This is a 2.5 order closure scheme as defined by *Mellor and Yamada* [1982], and more fully described by *Hong and Pan* [1996].

Despite its name, this module deals with vertical diffusion for heat, momentum and tracers both in the PBL and in the free atmosphere. It is a nonlocal diffusion scheme, in that within the PBL the tendency of mixed quantity, C , is calculated as

$$\partial C/\partial t = \partial/\partial z [K_c(\partial C/\partial z - \gamma_c)]$$

as by *Troen and Mahrt* [1986], with γ_c accounting for nonlocal effects which may have an important effect in this region (such as large-scale eddies). The diffusion coefficient, K_c is defined using the “local-K approach” of *Louis* [1979] in the free atmosphere, and using Monin-Obukhov similarity theory within the PBL, with γ_c proportional to the mean vertical eddy flux of the variable being dealt with (momentum, potential temperature, tracer amount, etc.) divided by a velocity scale (see *Hong and Pan* [1996] for details).

[25] The theory behind the PBL and free atmosphere parameterizations described here is thought to be universal to all fluids and thus likely to apply to any atmosphere. Indeed, it has been common practice to use such schemes in planetary dynamical models and as the basis of one-dimensional PBL models [e.g., *Haberle et al.*, 1993a]. We will present a comparison between MarsWRF results (in 1-D and LES modes) and observations of the Martian boundary layer, as well as other published model simulations, in a future paper.

4. Validating the Global WRF Model

[26] Before proceeding to use planetWRF for scientific applications, it was necessary for us to test our global modifications to the dynamical core, first in the absence of physical parameterizations (radiative forcing, boundary layers, moisture microphysics, etc.) to look at its basic advection performance (section 4.1), then using simplified physics representative of an Earth-like atmosphere to compare with other models (section 4.2). The absence of planetary-specific modifications in these cases also allowed us to isolate potential problems with the “globalizing” half of the changes needed to create planetWRF. All of the global simulations presented in this section were conducted in hydrostatic mode.

4.1. Basic Tests of the Dynamical Core

[27] Our basic performance tests for the global dynamical core were designed to ensure that the model is capable of allowing the global propagation of long wavelength gravity waves (section 4.1.1), and maintaining the advection of a discrete tracer over the pole (section 4.1.2). For these simulations, the model is set up with no planetary rotation (i.e., the Coriolis parameter, $f=0$), no radiative forcing, no boundary layer, surface layer or subsurface physical parameterizations, no parameterized diffusion, and using terrestrial physical constants.

4.1.1. “Ping” Test

[28] The first test starts the model with zero initial wind everywhere. In the absence of perturbations, this unforced model would thus remain in a state of zero flow indefinitely.

In this test, we examine the propagation of a wave away from an initial perturbation, with a dynamical time step of 30 s. The horizontal grid is 128×72 points, giving resolutions of 2.8125° and 1.25° in longitude and latitude, respectively, with 40 vertical levels equally spaced in eta (see definition in section 2). The propagation of the wave over the poles and the geometry of wave radiation in the spherical domain are of particular interest. Figure 2 shows the evolution of the gravity wave radiating from a 5% initial perturbation to the column mass field. “mu” is the perturbation column mass field (in kg/m^2) multiplied by acceleration due to gravity (assumed constant), thus has units of Pa. The initial perturbation is 5000 Pa (over a column total of 10^6 Pa) at a grid point just south of the equator (there is no “mass point” on the equator in this simulation’s grid). The “ringing” behind the first wavefront results from the generation of additional gravity wave sets by the continuing damped oscillation of the initial perturbation around the equilibrium pressure. That the original perturbation is a single grid-box, and hence is square, results in the propagation of a somewhat noncircular leading wavefront. However, the leading wavefront arrives at the antipode simultaneously regardless of which great circle route has been taken, and the antipodal rebound is both circular and confined. Thus there appears to be little anisotropy introduced into the domain by the shift to nonconformal geometry. Further, the propagation of the wavefront over the pole appears to result in no significant wave reflection or distortion. Note that the amplitude of the gravity waves diminishes greatly in the first few minutes of the simulation from geometrical spreading of the waves (peak pressures drop from 5000 Pa to about 200 Pa). After that, the amplitudes of the perturbations decrease much less rapidly, since only resolved mixing and inherent numerical diffusion is at work (i.e., no sub-grid-scale parameterized diffusion is active).

4.1.2. “Over the Pole” Test

[29] In our second test, a “cosine hill” initial tracer field is advected over the model pole by winds in constant solid body rotation over the pole of a nonrotating planet. The simulation uses a 600 s time step, uses a grid of 256 (longitude) by 128 (latitude) points giving an equatorial grid spacing of about 156 km, and has peak winds of about 57 m/s. The constant wind field and the evolution of the passive tracer are shown in Figure 3. The subfigures shown are not evenly spaced in time, but rather are chosen to emphasize particularly interesting events over the course of a single rotation, as the cosine hill is advected due north from the equator following the 90 degrees east meridian, then due south following the 90 degrees west meridian, then over the south pole and finally back to its initial position. Since peak flow occurs along lines intercepting the poles, this simulation maximizes the impact of polar errors, and the minimal change in the shape of the hill after one rotation demonstrates that advection errors at the poles are not of concern.

4.2. Held-Suarez Test of a Dynamical Core

[30] The basic diagnosis of dynamical core behavior using the simplified prescribed forcing suggested by *Held and Suarez* [1994] (hereafter HS94) has become a standard

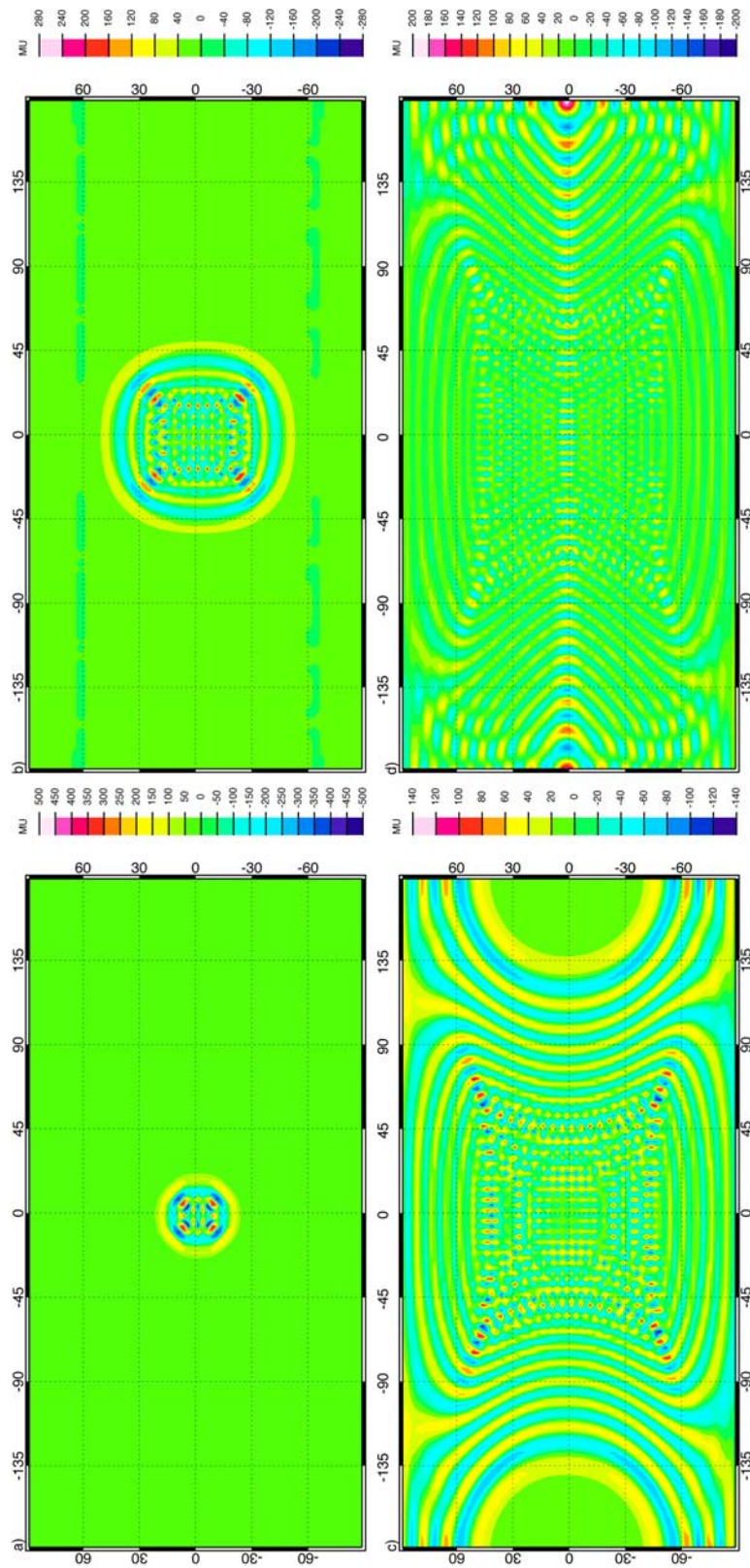


Figure 2. The evolution of a gravity wave radiating from an initial single point column mass perturbation of 5%. Here mu is the perturbation column mass field (in kg/m²) multiplied by the acceleration due to gravity (assumed constant) and thus has units of Pa. Figure 2a shows mu a short time later, and Figure 2b shows mu shortly before the leading wavefront reaches polar regions. The bottom plots show mu after the leading wavefront has progressed over both poles (Figure 2c) and as it reaches the antipodal point 180° in longitude around the planet (Figure 2d).

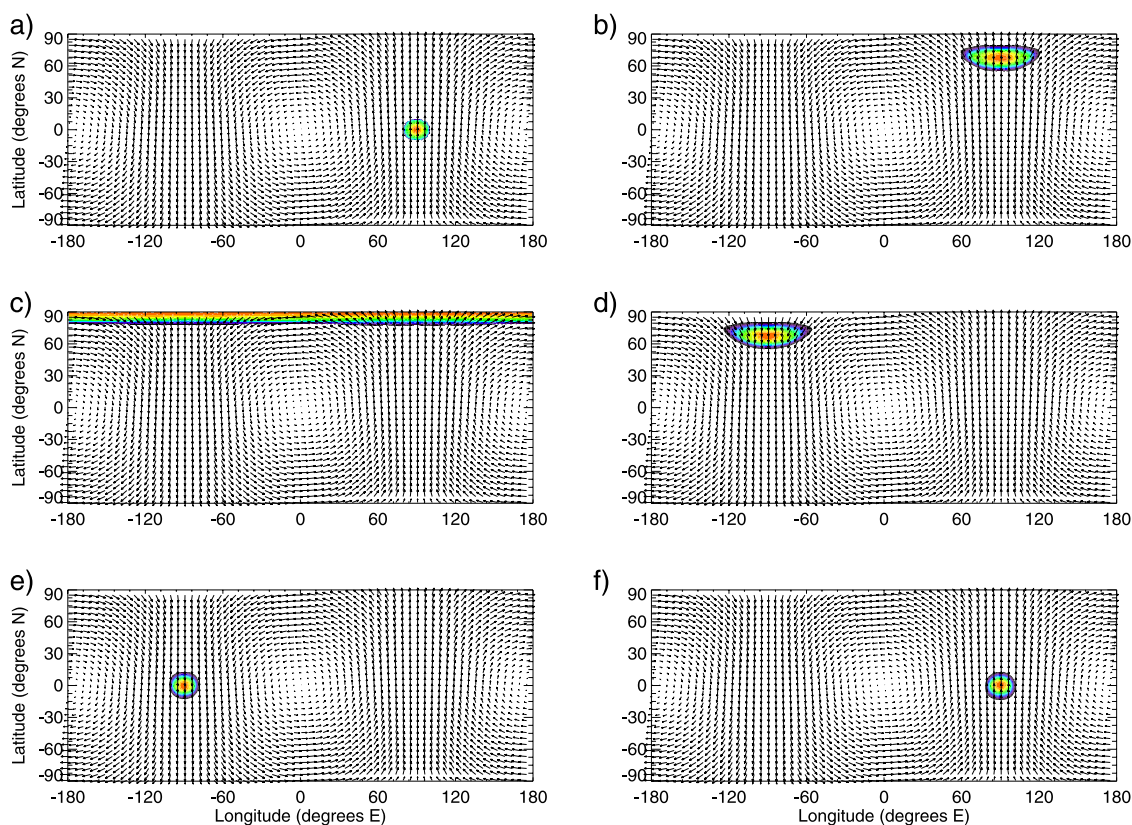


Figure 3. Advection of a “cosine hill” tracer distribution (shaded) by winds (arrows) in solid body rotation over the poles of a nonrotating planet. Figure 3a shows the initial tracer distribution, and Figure 3f shows the result after one complete rotation, with Figures 3b through 3e chosen to show interesting events in between (rather than being evenly spaced in time). For clarity, only every fourth wind vector is shown, and the longest vector length corresponds to approximately 57 m/s.

test for new models (see, for example, a citations list for HS94). HS94 provides “benchmark” simulation results from two global models (one grid point and one spectral) using highly simplified parameterizations of atmospheric heating (Newtonian relaxation to a prescribed temperature profile) and boundary layer friction (Rayleigh damping of low-level winds). The results consist of long-term averages (1000 days, following a 200 day spin up) of zonal-mean zonal winds and temperatures, and some eddy statistics. It should be noted that these results cannot be thought of as “exact” solutions for the prescribed forcings, as the models used by HS94 produce slightly different results for different numerical approaches, different model resolutions, and order of advection used. They do, however, provide an extremely useful means of intercomparing different approaches to integration of the same basic equations, as shown in HS94 and in papers by other authors who have performed these tests [e.g., *Chen et al.*, 1997; *Fox-Rabinovitz et al.*, 1997; *Lin*, 2004; *Dowling et al.*, 2006]. There is generally very good agreement between results for different dynamical schemes, provided the same resolutions and parameter values are used.

[31] Here, we show and describe a simulation using the HS94 forcing with resolution closest to those shown in HS94 (in our case, a mesh of 72 points in latitude, 128 in longitude, with 20 vertical levels, henceforth the WRF-

HS94 simulation). The results are for the final 1000 days of a 1200 day simulation.

[32] The spin-up phase of the WRF-HS94 simulation is shown in Figure 4. Initially, the model solution is zonally symmetric, with the winds steadily increasing. Indeed, we found that the global version of WRF is capable of achieving a steady state, zonally symmetric solution and maintaining it for multiple years. This is a valid solution, but one that differs markedly from the HS94 results; it demonstrates the very low degree of internal noise and dissipation in the global WRF dynamical core. In order to achieve a more geophysically meaningful solution, we found that a very small amount of initial noise was needed to seed zonal perturbations and the development of midlatitude turbulence. The development of this turbulence, and a snapshot of the global “weather patterns” at one year into the simulation, are shown in Figure 4.

[33] Since the prognostic equations in WRF’s dynamical core are formulated in terms of variables that have conservation properties (e.g., density-weighted winds and potential temperature) [*Ooyama*, 1990; *Wicker and Skamarock*, 2002; *Skamarock et al.*, 2005], the global WRF dynamical core should retain the same conservation properties. Figure 5 shows the percentage change in (a) total atmospheric mass and (b) angular momentum as a function of time in an extended (15 year) WRF-HS94 simulation.

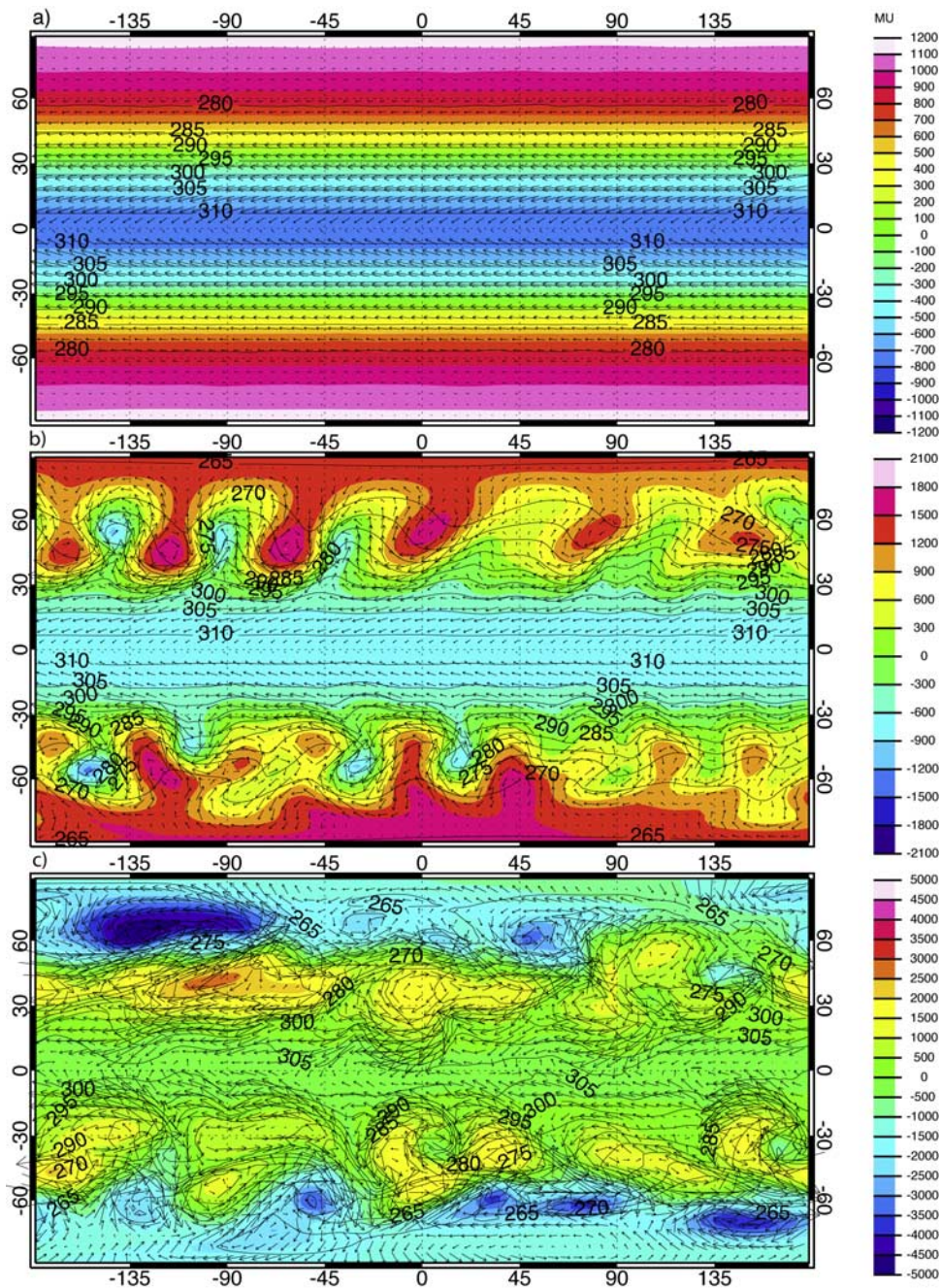


Figure 4. The onset of eddies in the WRF Held-Suarez simulation. In each subfigure the surface pressure perturbation, near-surface air temperatures, and near surface wind vectors are shown as background coloring, black contours, and black arrows, respectively. (a) The initially zonally symmetric fields (at 30 days after the start of the simulation) yield to (b) the development of quasiperiodic instabilities in the midlatitude jets (60 days into the simulation), which (c) ultimately settle into steady state turbulence involving baroclinic frontal storm systems (shown here at 1 year into the simulation).

The total mass fluctuates by less than $\pm 0.015\%$, and angular momentum by less than about 0.1% , over these 15 years, and neither shows any long-term trend. Thus the global WRF model retains the conservation properties of the original WRF model.

[34] Figure 6 shows the global WRF results for zonal-mean temperature and zonal-mean zonal wind as a function of height, averaged over the last 1000 days of the 1200-day

WRF-HS94 simulation. These results have been plotted to be directly comparable to the results shown in HS94. The thermal structure (Figure 6a) compares very well with the HS94 grid point model (HS94, Figure 1c) roughly below the 0.25 sigma level. In the tropical atmosphere above this level, the temperatures are also in good agreement. In the region of very weak vertical temperature change in the extratropics above the 0.25 sigma level, the global WRF

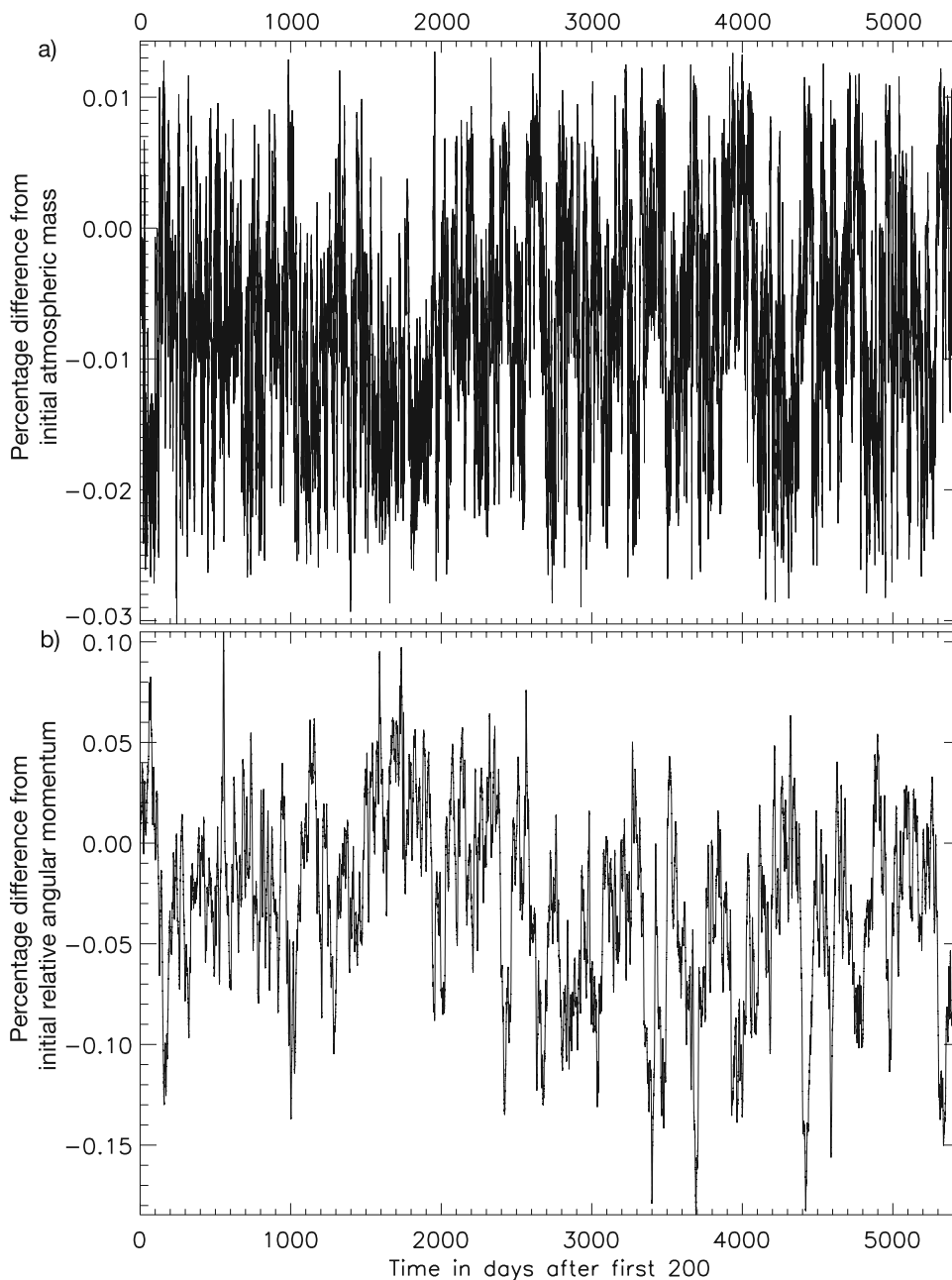


Figure 5. Percentage change in (a) total atmospheric mass and (b) angular momentum over 15 years of the extended WRF-HS94 simulation, demonstrating no long-term trend and minimal fluctuations.

model shows slightly more structure in the transition from 215 to 205 K. This may be associated with the stronger zonal winds in the upper polar atmosphere in global WRF versus the two models shown by HS94 (compare our Figure 6b with Figure 2 of HS94). Throughout the atmosphere below the 0.25 sigma level, the agreement in temperature structure and values are excellent (for example, the 260 K contour crosses the equator at a sigma of 0.5, and reaches the pole at a sigma of 0.85, in all cases).

[35] Since the thermal and zonal wind fields are tightly coupled, it is not surprising that the global WRF dynamical core agrees as well with the HS94 prediction of zonal-mean zonal wind as it does for temperature (Figure 6b versus

Figure 2 of HS94). The jet cores in the extratropics at roughly 45° are located at a similar height (about the 0.3 sigma level) and have a similar peak speed (just over 28 m s^{-1}) to those simulated by HS94. Tropical surface easterlies peak above 8 m s^{-1} , with peak surface westerlies in the midlatitudes near $45\text{--}50^\circ$ at above 6 m s^{-1} , and are also highly consistent with HS94.

[36] Global WRF thus performs well in terms of the zonal mean climatology. Although this suggests that eddy transports are reasonable, we have also directly compared the eddy statistics with those from the HS94 models. Figure 7 shows (a) the time-averaged eddy variance of temperature and (b) the time and vertical mean of the zonal spectra of the

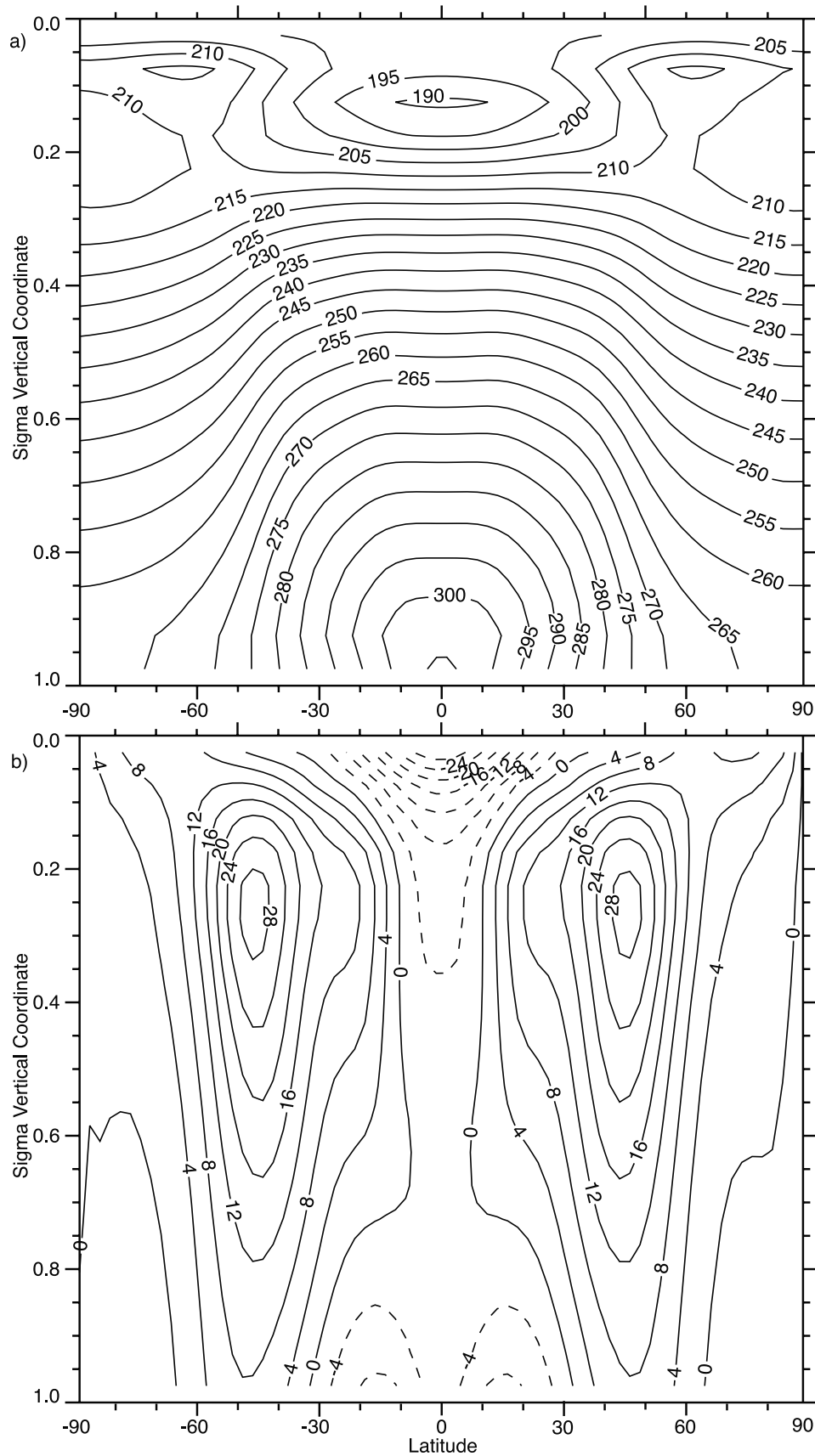


Figure 6. Zonal-mean (a) temperatures in Kelvin and (b) zonal winds in m/s averaged over the last 1000 days of the 1200-day WRF-HS94 simulation. The vertical axis in both plots is eta (almost exactly the same as sigma in these hydrostatic simulations for which P_{top} is almost zero).

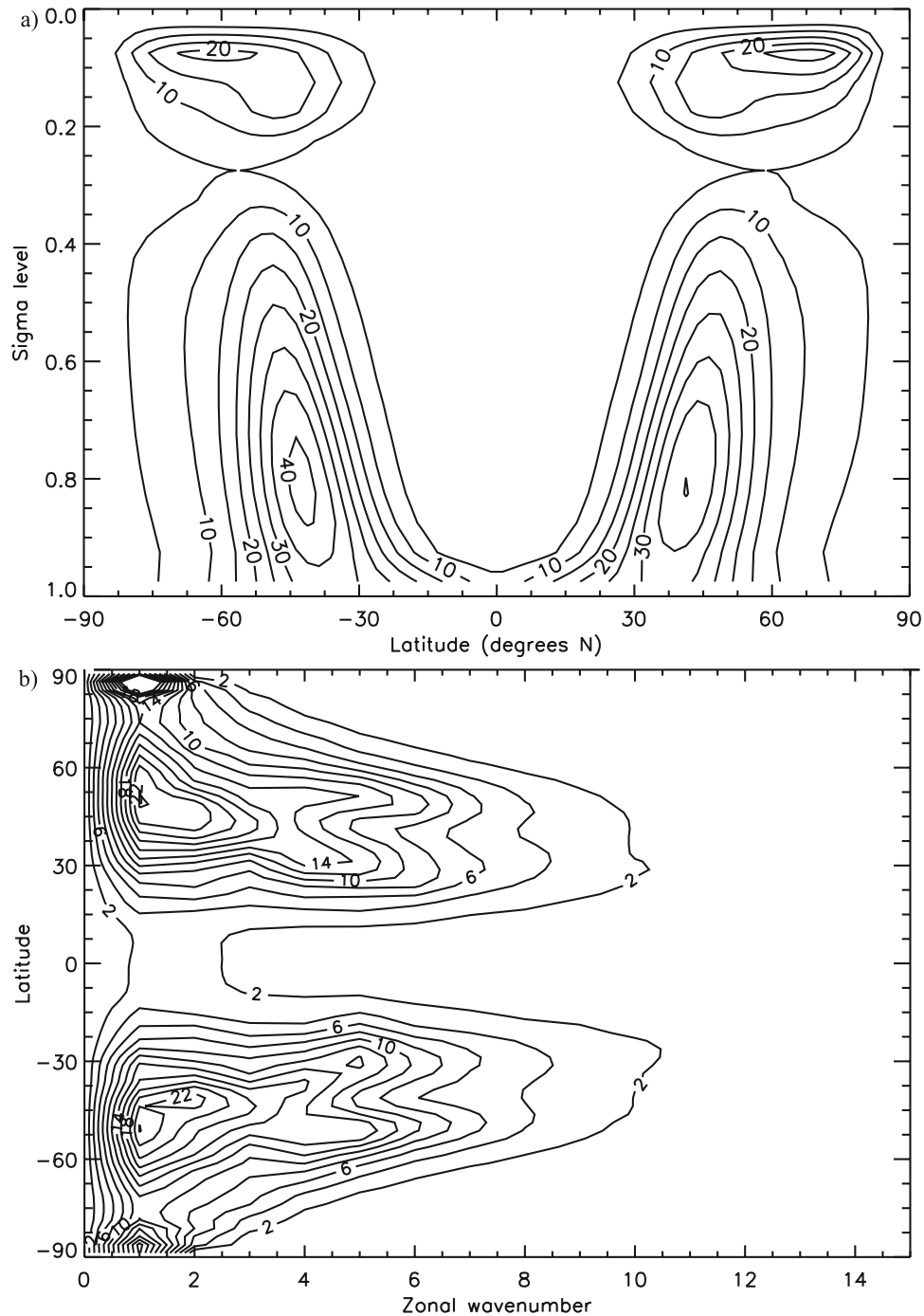


Figure 7. (a) Eddy temperature variance [K^2] and (b) vertically averaged zonal spectra of the eddy variance of zonal wind [$m^2 s^{-2}$] averaged over the last 1000 days of the Held-Suarez simulation.

eddy variance of zonal wind. These can be compared with HS94 Figures 3 and 4. The eddy temperature variance (Figure 7a) compares very well in both shape and magnitude with both HS94 models, and especially the grid point model (WRF is more similar to the HS94 grid point model in the upper domain in the high latitudes, where the variance falls off at the upper boundary). WRF typically has higher eddy temperature variance right at the poles than either the HS94 grid point or spectral models. For the eddy variance of zonal wind (Figure 7b), the agreement is also good, with peak magnitudes of $20 m^2/s^2$ at zonal wave number 2

between 40° and 50° latitude, and of about $12 m^2/s^2$ at zonal wave number 5 with a double peaked structure in midlatitudes.

5. Planetary WRF Model

[37] In the last section we described validating our global changes (basically the use of nonconformal map projections and polar boundary conditions), while the model was still terrestrial. In this section, conversely, we show results from the version of WRF modified to simulate other planets'

atmospheres, but for two nonglobal cases (using the original conformal map projections and equations). We thus focus on the new model's planetary capability by presenting results from two nonglobal planetWRF simulations, using features intrinsic to the original WRF model that remain accessible within planetWRF. Section 5.1 shows results from a large eddy simulation of convection under Mars conditions, and section 5.2 shows results from a mesoscale simulation (with periodic horizontal boundary conditions) of the Valles Marineris region on Mars. The large eddy simulation was conducted using the nonhydrostatic version of planetWRF, and the mesoscale simulation with the model in hydrostatic mode.

5.1. Large Eddy Simulations of Convection in the Martian Boundary Layer

[38] A large eddy simulation (LES) uses a numerical model with sufficient resolution to explicitly simulate the larger eddies involved in boundary layer convection [e.g., *Stevens and Lenschow*, 2001]. LES methods have only recently begun to be applied to Mars as a limiting case application of mesoscale/microscale models [*Rafkin et al.*, 2001; *Toigo et al.*, 2003; *Michaels and Rafkin*, 2004], although two-dimensional resolved models slightly predate them [*Odaka et al.*, 1998]. Prior to this (and still of great value), the boundary layer was studied using parameterized one-dimensional models [e.g., *Haberle et al.*, 1993a; *Määttänen and Savijärvi*, 2004].

[39] WRF is amenable to LES application since it uses fully compressible, nonhydrostatic governing equations of motion. The NCAR-released version of WRF required only modification of the surface layer model and dynamical core to allow surface layer drag and heat flux between the surface and atmosphere in the absence of a parameterized PBL scheme (such as the MRF PBL; see section 3.4.4). While the LES WRF is designed to capture a large fraction of the turbulent eddy spectrum, computational reality still dictates a resolution too poor to capture the viscous or inertial subranges (i.e., LES WRF uses grid spacings of at least a few meters). Sub-grid-scale parameterization of diffusion is thus still needed, and WRF follows the somewhat standard three-dimensional deformation approach of *Smagorinsky* [1963]. As designed, in LES mode, the model is capable of being forced by a background wind of specified magnitude and direction. We have also added the capability of forcing the model with a large-scale slope model, as defined by *Haberle et al.* [1993a]. Comparisons between the MarsWRF LES, previous modeling studies, and data collected at the various Mars landing sites are deferred to a future paper. Here, we merely present illustrative results.

[40] Results from an example MarsWRF LES are shown in Figures 8 and 9. This simulation has a domain extent of 300 grid points in both horizontal directions and 100 in the vertical. With 100 m horizontal grid spacing, the domain thus covers 30 km by 30 km. In the vertical, an increasingly stretched grid covers 10 km, with the lowest layer about 20 m in thickness and with layer thicknesses increasing with height. The domain is doubly periodic, with no horizontal variations in topography (elevation corresponding to a surface pressure of 830 Pa, with surface roughness of 1 cm), albedo (0.32), or thermal properties (thermal

inertia = $290 \text{ J m}^{-2} \text{ s}^{-1/2} \text{ K}^{-1}$, unit emissivity). The simulation shown has a uniform Coriolis parameter corresponding to 22°N , and has been run for $L_s = 45^\circ$. A uniform background wind of 7 m s^{-1} is applied to the entire horizontal domain at all heights.

[41] The evolution of the horizontal structure of convection during the morning is shown in Figure 8. Variations in the potential temperature highlight the presence of convection cells that are defined by relatively thin, warm, upwelling sheets (the walls of approximately hexagonal convective cells), and much more expansive, cooler downwelling. This pattern is that of open cellular convection. Following the evolution near the surface (the roughly 9 m level is shown), the scale of the largest cells grows in the period from 8 AM to noon, from roughly 3 km to 10 km. Smaller cells on scales down to less than a kilometer are evident even in the noon snap-shot. Looking at the horizontal slice at an altitude of 1 km, the larger-scale cells are represented, but the smaller cells have largely been filtered out.

[42] Vertical slices through the model at the middle of the domain are shown in Figure 9 for the same times as shown in Figure 8, with the addition of 11 AM. In this representation, the evolution appears more consistent with the development of penetrative warm plumes. Near the surface, multiple plumes develop associated with the unstable environment, of which only some penetrate to great vertical extent. These plumes are the upwelling cellular sheets or walls evident in Figure 8. The evolving warm and cool perturbations are reminiscent of the continuous Mini-TES observations from the Mars Exploration Rovers (MER), as shown by *Smith et al.* [2004], and will be discussed further in a future paper.

[43] The reduction in the number of plumes penetrating to greater heights is directly associated with the filtering of small-scale cells with height in the horizontal plots. At the lowest levels, cells of various sizes are generated and these cells develop aspect ratios of between roughly 1 and 5, consistent with terrestrial boundary layer convection. Cells of small horizontal scales thus have correspondingly small vertical scales, and simply do not constitute part of the spectral population of cells at greater height. The action of the larger cells in "eroding" the stable layer above the convective boundary layer is highlighted in Figures 9c and 9d, where the penetration of plumes into the stable layer, and entrainment and downward transport of air from this layer is evident. The growing depth of the convective PBL during the morning is also obvious from these plots. Given a convective PBL depth of about 5 km by noon, the maximum sized 10 km horizontal cells suggests a large eddy aspect ratio of about 2. The absence of larger structures in a domain of roughly 9 times the area of the largest evolved cell suggests that the model extent is not arbitrarily restricting the expressed horizontal extent of convection.

5.2. Mesoscale Simulations of Flows Through Valles Marineris on Mars

[44] An idealized simulation of flow in Valles Marineris is illustrated in Figure 10. The simulation is idealized in the sense that the domain is set to be doubly periodic, the local time is defined to be identical at all grid points on any given time step, and the Coriolis parameter is set to a uniform value across the domain. Our goal with the simulation was

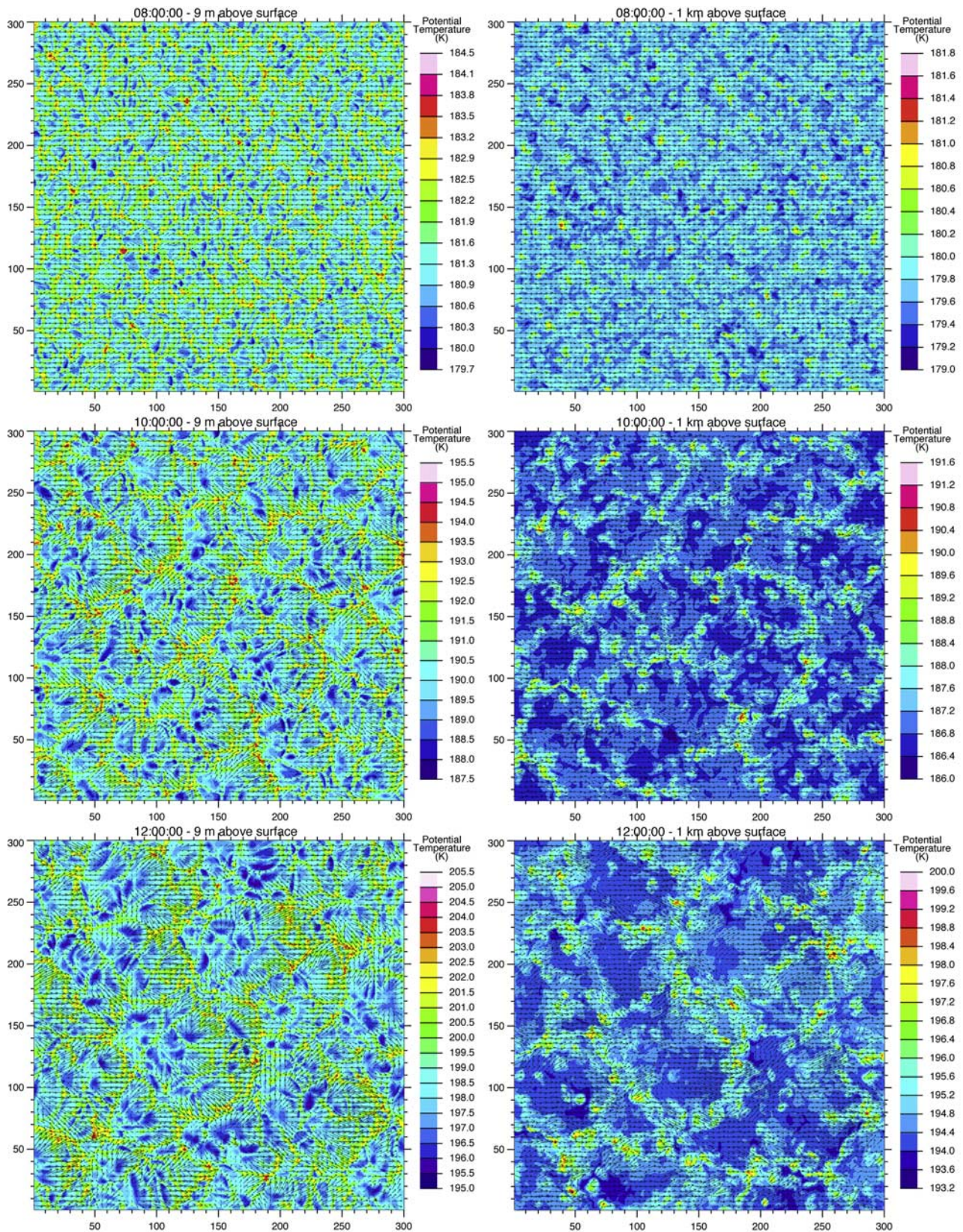


Figure 8. The growth of convective cells over 3 hours in a 300×300 large eddy simulation (LES) for Mars conditions. The plots on the left show potential temperature at a height of approximately 9 m, while those on the right show it at a height of approximately 1 km. The top row is at 8 AM local time, the middle row is at 10 AM local time, and the bottom row is at local noon. Note that the contour intervals vary from plot to plot.

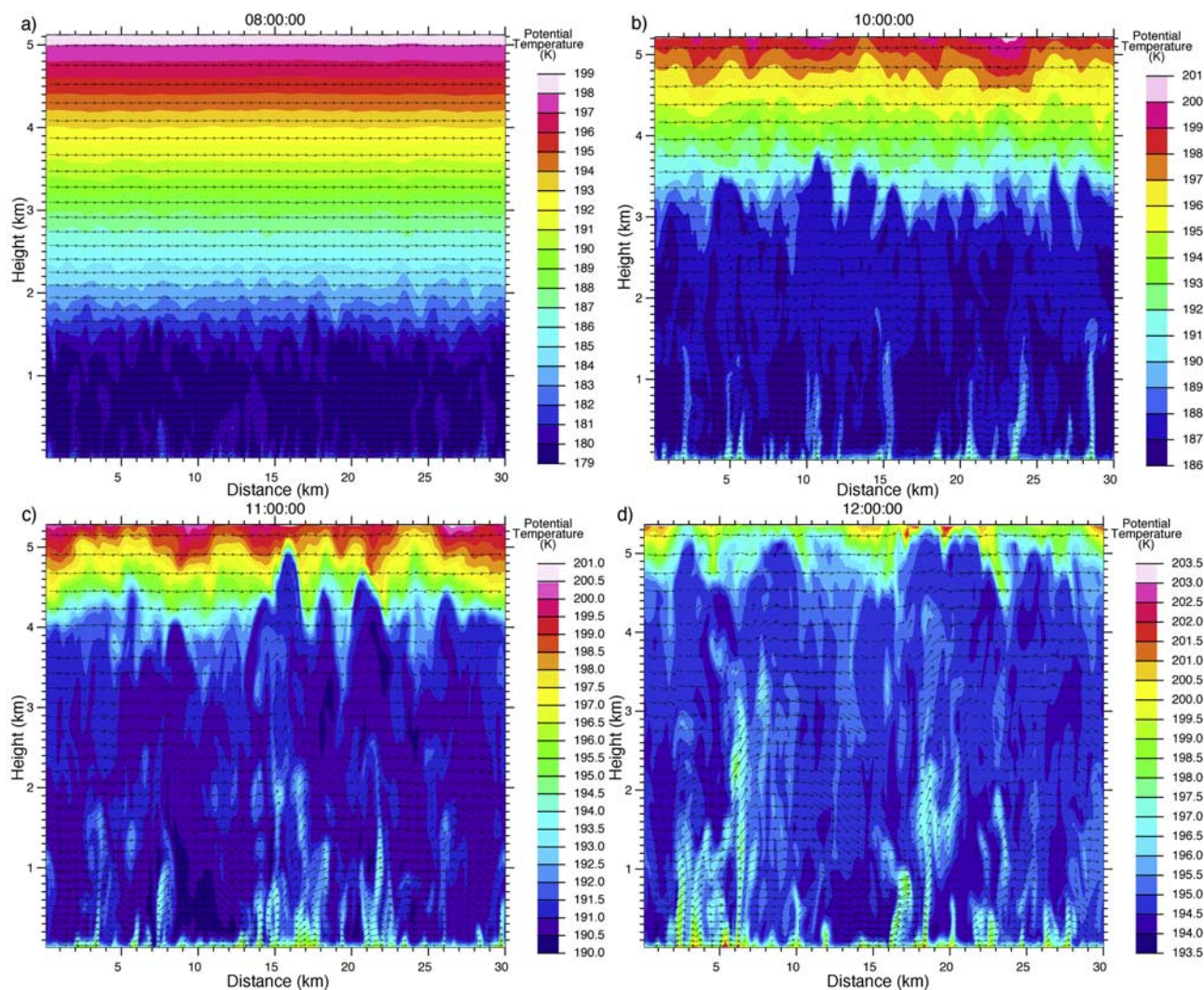


Figure 9. Potential temperature as seen in a vertical slice through the center of the domain. Local times shown are (a) 8 AM, (b) 10 AM, (c) 11 AM, and (d) 12 PM. The model domain actually extends up to 10 km in height; thus only the lower half is shown here.

to examine slope flow on the canyon walls in the absence of local time variations and the influence of larger-scale flows. There is no large-scale background wind applied. The domain comprises 60×120 grid points in the horizontal (24 km spacing), with 25 vertical levels extending up to ~ 40 km. The vertical grid spacing (in eta coordinates) increases steadily toward the model top, with the 26 half levels defined by $1 - [(k - 1)/25]^{1.3}$, where $k = 1$ denotes the surface and $k = 26$ the model top.

[45] Valles Marineris provides one of the most significant regions of topographic relief on Mars. The canyon walls have been shown in previous mesoscale simulations to be associated with significant buoyancy-driven upslope/downslope winds [Rafkin *et al.*, 2001; Toigo and Richardson, 2003]. Figure 10 shows four local time snapshots of wind at the lowest model level (at approximately 80 m altitude). The simulation confirms the generation of upslope and downslope winds on the canyon walls of up to several m/s during the times of peak daytime heating and after sunset, respectively. These winds are particularly strong in the sector north of Coprates Chasma (to the east of the maximum

north-south width of the canyon system). Flow inside the canyon is driven along the canyon axis, with generally downslope (east-to-west) flow at night and upslope flow during the daytime.

6. Planetary, Global WRF Model

[46] Here we present results from global versions of planetWRF for Mars, Titan, and Venus. Detailed validation and study of the various planetary WRF GCM simulations will be shown in future papers. Here, we merely present basic results that allow an overview comparison with available data sets and other published models. For Mars, we additionally show simulations undertaken with the computational poles offset from the geographical poles (a “rotated pole,” or transverse cylindrical projection, simulation), demonstrating that the computational geometry does not deleteriously affect the zonal mean circulation and thermal structure. All of the simulations presented in this section were conducted in hydrostatic mode. The default horizontal resolution of the planetWRF GCM is 36 equally

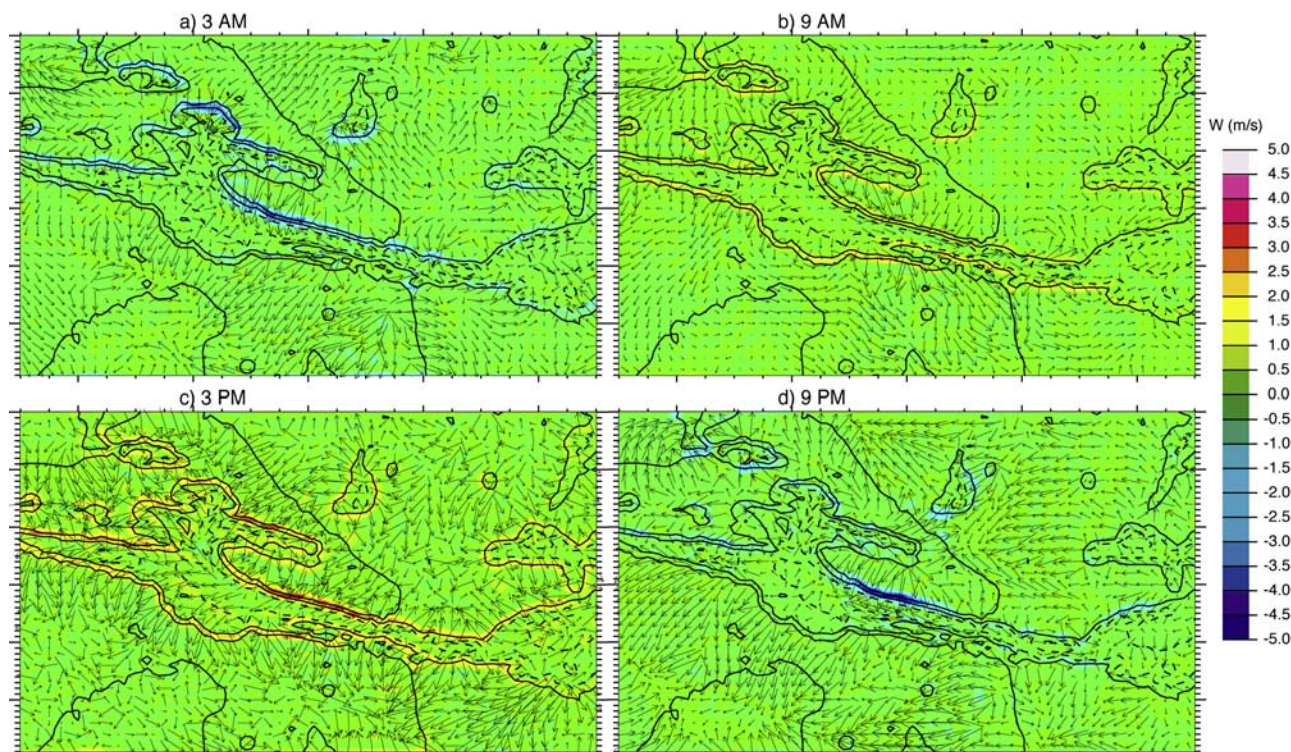


Figure 10. The diurnal cycle of winds in the Valles Marineris region on Mars, simulated by MarsWRF run as a mesoscale model with periodic horizontal boundary conditions. The background color shows vertical wind, and the arrows show horizontal wind (though only one in four wind vectors is shown for clarity). Local times shown are (a) 3 AM, (b) 9 AM, (c) 3 PM, and (d) 9 PM. Unlabeled topography contours are shown for geographical reference.

spaced grid points in latitude by 64 equally spaced grid points in longitude, although (where mentioned) other resolutions can and have been used.

6.1. Global MarsWRF Results

[47] The main goal of the initial testing of the MarsWRF GCM was to confirm that the general circulation generated by the model agrees with other models and with observations to within the spread of uncertainty in current GCM simulations, and to probe the importance of resolution and the location of the model numerical pole. The zonal-mean temperature structure and the zonal-mean zonal wind as simulated by the MarsWRF GCM standard simulation are shown for the two solstices and for northern autumnal equinox in Figures 11 and 12. The cross sections of temperature are directly comparable to retrievals from TES data for the first MGS mapping year [Smith *et al.*, 2001], using an averaging interval of 5° of L_s . The simulations use the “MGS scenario” dust opacity prescription defined for the LMD/Oxford Mars Climate Database (see section 5.1.1). We use the same vertical levels as those of Lewis *et al.* [1999, Table 3], with fine resolution in the planetary boundary layer increasing toward the surface (e.g., with 4 layers below 100 m), and a resolution of about half a scale height above this (until the more widely spaced sponge layers are reached). The top model layer is at a height of ~ 100 km. The output compare very well in both distribution and magnitude with the data, and the degree of agreement and reasons for the quality of the agreement will be discussed in a future paper. As also shown by Wilson *et*

al. [2006], the MarsWRF GCM produces zonal wind and temperature distributions that agree well with other published models. This agreement is predominantly a test of the dynamical core, since the physical forcing very closely follows the schemes used in the LMD/Oxford models.

[48] Two model resolutions are shown for the traditional GCM configuration. As mentioned above, the standard resolution thus far used for the planetWRF GCM has 36×64 grid points in the horizontal. In all cases shown in this section, the 25 layer vertical structure of the Oxford/LMD model is used, although we have also conducted simulations with the 40-layer GFDL model structure, yielding similar results to those shown. Also shown in Figures 11 and 12 are “high-resolution” simulations at 135×256 horizontal resolution (or $1.333^\circ \times 1.4^\circ$). In all cases, the panels shown are from at least several years into a simulation. The output shows that the increased resolution does not dramatically change the zonal mean atmospheric structure and circulation.

[49] The right-hand columns of Figures 11 and 12 show results from a simulation in which the computational poles have been placed on the geographical equator. This transverse cylindrical projection is illustrated in Figures 13a–13d, with the mathematical definition (taken from Suarez and Takacs [1995]) being provided in Appendix C. This projection has the advantage of providing good and uniform resolution at the geographical poles, which should be of great use for simulation of the crucial Martian polar regions. Figures 11 and 12 show that the zonal mean atmosphere simulated using the “rotated pole” orientation is not sig-

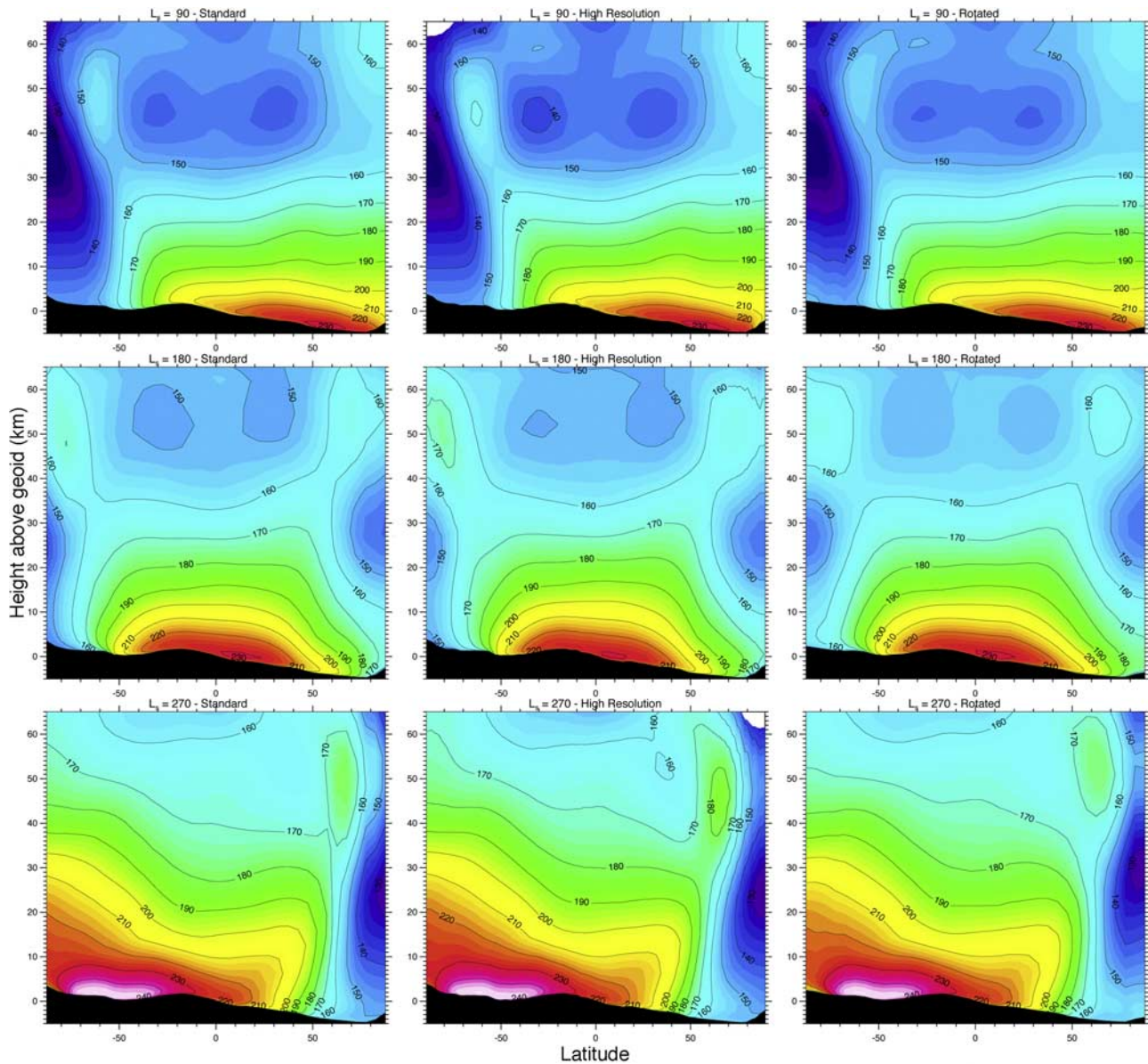


Figure 11. Zonal-mean temperatures in K (background color and contour lines) from a series of global MarsWRF simulations using the MGS dust scenario (see text). The top row shows results at $L_s = 90^\circ$, while the middle row shows $L_s = 180^\circ$ and the bottom row shows $L_s = 270^\circ$. The left column shows results from the standard MarsWRF global setup (see text). The middle column shows results from a simulation run at twice the horizontal resolution. The right column shows results from a global simulation using the transverse cylindrical map projection.

nificantly different from that generated with a traditional GCM computational grid (note that the output from the “rotated pole” MarsWRF GCM was rotated into traditional simple cylindrical projection before zonal averaging). Martian topography aids in the use of the rotated pole grid by providing rather uniformly flat regions on the equator at the prime meridian and the date line that are convenient places to locate the computational poles. Figures 13e–13h show winds over the southern hemisphere only, for southern winter (Figures 13e and 13f) and summer (Figures 13g and 13h). Results are shown from both standard (Figures 13e and 13g) and rotated pole (Figures 13f and 13h) simulations, with the standard model results projected onto the rotated pole

grid for ease of comparison. The south pole is in the center of each plot, with the axes labeled by grid point. Within a few grid points of the pole the circulation patterns can be quite different between the two simulations, whereas further equatorward the patterns are quite similar even though the wind speeds are different in some locations.

6.2. Global TitanWRF Results

[50] The initial goals of the TitanWRF GCM simulations described here were to “spin-up” a model state under full seasonal and diurnal forcing, and to compare the zonal mean circulation with observations and other models. The simulation was started with zero winds and with the

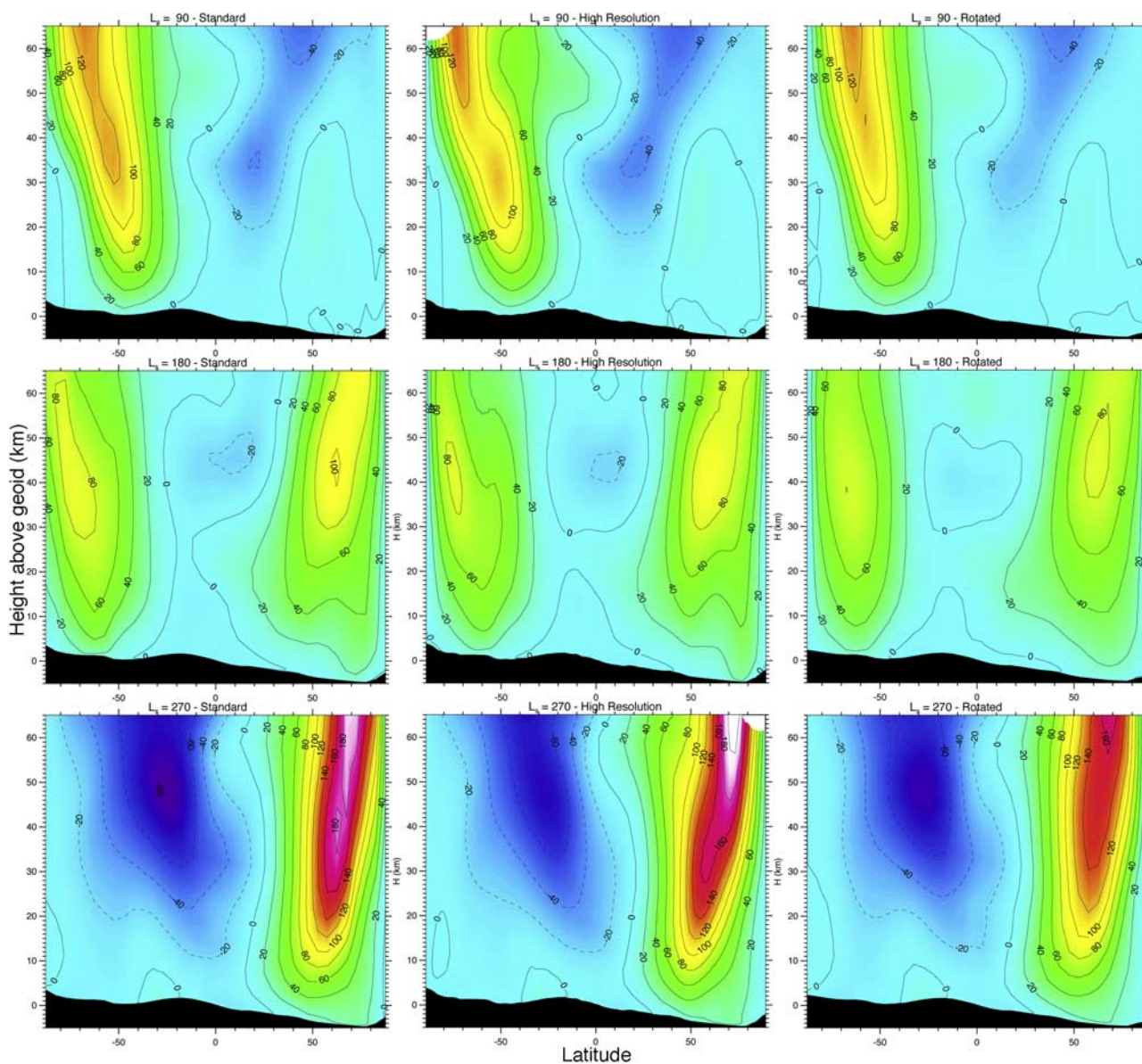


Figure 12. As in Figure 11 but showing zonal-mean zonal winds in m/s.

Lellouch et al. [1989] temperature profile applied everywhere. The standard 36×64 horizontal mesh has been used, along with 55 vertical levels (following *Hourdin et al.* [1995], the vertical levels were almost equally spaced in log-pressure except near the surface and the model top at ~ 400 km). In addition to the standard thermal forcing and mechanical damping, described in section 3.4, the winds in the top four model layers were damped on timescales of 1, 2, 4 and 6 Titan days (the timescale in this “sponge layer” decreased toward the model top). The simulation ran for 15 Titan years, by which time it had apparently reached the end of its “spin up” phase (net annual exchange of angular momentum with the surface had essentially ceased). The total atmospheric mass was conserved to within $\pm 0.03\%$ over the duration of the simulation, with no long-term trend.

[51] Figure 14 shows the evolution of the superrotation index within four different atmospheric layers during the model spin-up. Superrotation index is the total angular momentum divided by that of an atmosphere at rest with

respect to the planet’s surface. By the end of spin-up, the TitanWRF GCM obtains a superrotation index of only ~ 3 in the 0–2 mbar region, lower than that inferable from the observed winds [*Flasar et al.*, 2005; *Folkner et al.*, 2006]. Overall, the TitanWRF GCM zonal winds are far weaker than those simulated by the LMD Titan GCM [*Hourdin et al.*, 1995] (who obtain a superrotation index of ~ 7), but stronger than those obtained by *Tokano et al.* [1999] (see below). It remains unclear why there is such spread in the maximum winds obtained by the models and this provides some doubt as to whether the mechanisms of atmospheric circulation on Titan are quantitatively understood.

[52] Figure 14 shows that each layer is superrotating, with a semiannual variation that is most apparent in the upper layers. As discussed by *Hourdin et al.* [1995], this variation is due to the different vertical transports of angular momentum during equinox and solstice, and can be illustrated with plots of the model mass stream function for equinox and

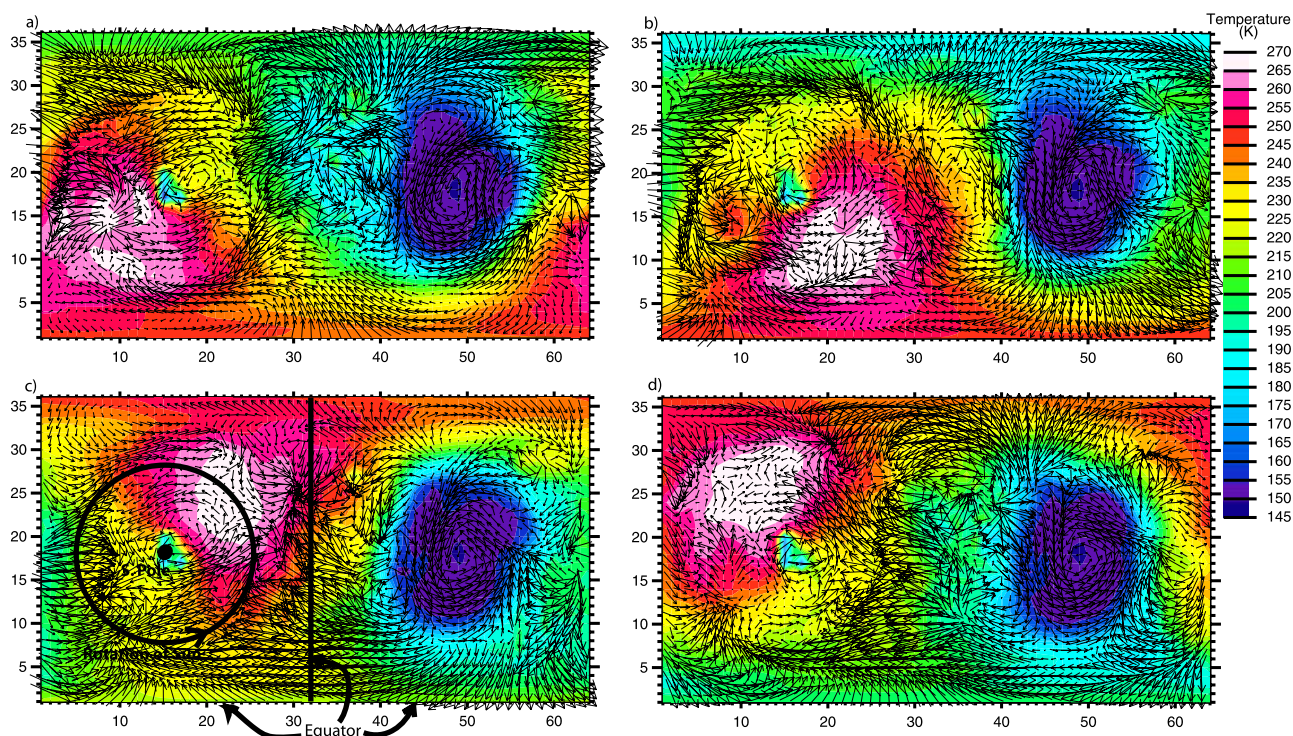


Figure 13. (a–d) The evolution of air temperature and winds at roughly 200 m in the computational grid of the rotated pole or transverse projection MarsWRF domain. The output are for $L_s = 270^\circ$ and local times at the prime meridian of (a) 9 AM, (b) 3 PM, (c) 9 PM, and (d) 3 AM. To aid interpretation of the projection, Figure 13c is annotated with the location of the southern pole, the sense of rotation of peak solar heating, and the location of the equator (the equator actually extends all the way around the outside of the figures, but only the bottom edge is annotated in c). The x and y axes are the grid point indices. (e–h) Winds at 6 km in the transverse plotting projection for the rotated pole and standard MarsWRF GCM simulations. The standard simulation has been reprojected onto the “rotated pole” grid (i.e., the inverse transformation of that undertaken in the construction of Figures 11 and 12.) Each plot shows essentially the left-hand portion of the maps shown in Figures 13a–13d, with the south pole located in the center. Southern winter ($L_s = 90^\circ$) is shown for (e) the standard model and (f) the rotated pole model. Southern summer ($L_s = 270^\circ$) is shown for (g) the standard model and (h) the rotated pole model.

solstice conditions, shown in Figure 15. Close to equinox, the circulation consists of two cells rising at the equator, which produces net upward transport of angular momentum within the troposphere and stratosphere. Around solstice, however, there is a single cell from the summer to the winter hemisphere, the downward branch of which passes through the strong stratospheric winter jet (see Figure 16b). The semiannual switching of these cells creates the alternating patterns of decreasing and increasing superrotation seen in Figure 14.

[53] Figure 16 shows zonal-mean zonal winds (top row) and zonal-mean temperatures (middle row) averaged over 10 Titan days for two times of year chosen to highlight maximum hemispheric symmetry (left column) and maximum hemispheric asymmetry (right column). Maximum asymmetry also corresponds to maximum zonal winds and superrotation index. These plots provide some insight into why the simulated superrotation is too low: namely, the equator-to-(winter) pole latitudinal temperature gradient in the lower stratosphere appears to be too weak. The variation in Figure 16d represents one of the largest gradients developed in the model, with a peak equator-to-pole difference of just 2.5 K at 300 Pa, which is small compared to a

greater than 20 K equator-to-pole difference in the real atmosphere [e.g., *Flasar et al.*, 2005]. In concert with the reduced thermal gradients, the modeled zonal winds are lower than observed. The model generates peak zonal winds of ~ 30 m/s at a few tens of Pa at latitudes ~ 50 – 65° S, but peak zonal winds of over 160 m/s have been inferred from temperatures measured by Cassini’s Composite Infrared Spectrometer [*Flasar et al.*, 2005].

[54] In order to test whether the mismatch in latitudinal temperature difference (and hence likely zonal winds) is due to the radiative forcing, we ran the TitanWRF model with all dynamics turned off; each latitude and longitude point then acts as a separate one-dimensional radiative convective model. In this case, strong equator-to-pole temperature gradients exceeding 90 K at 100 Pa were produced at solstice. This suggests that the meridional circulation produced in the TitanWRF GCM is very efficient at driving meridional heat transport, and largely destroys the thermal gradient. Similar behavior is noted by *Hourdin et al.* [1995] and *Tokano et al.* [1999], though despite this the *Hourdin et al.* [1995] model maintains temperature gradients of over 15 K.

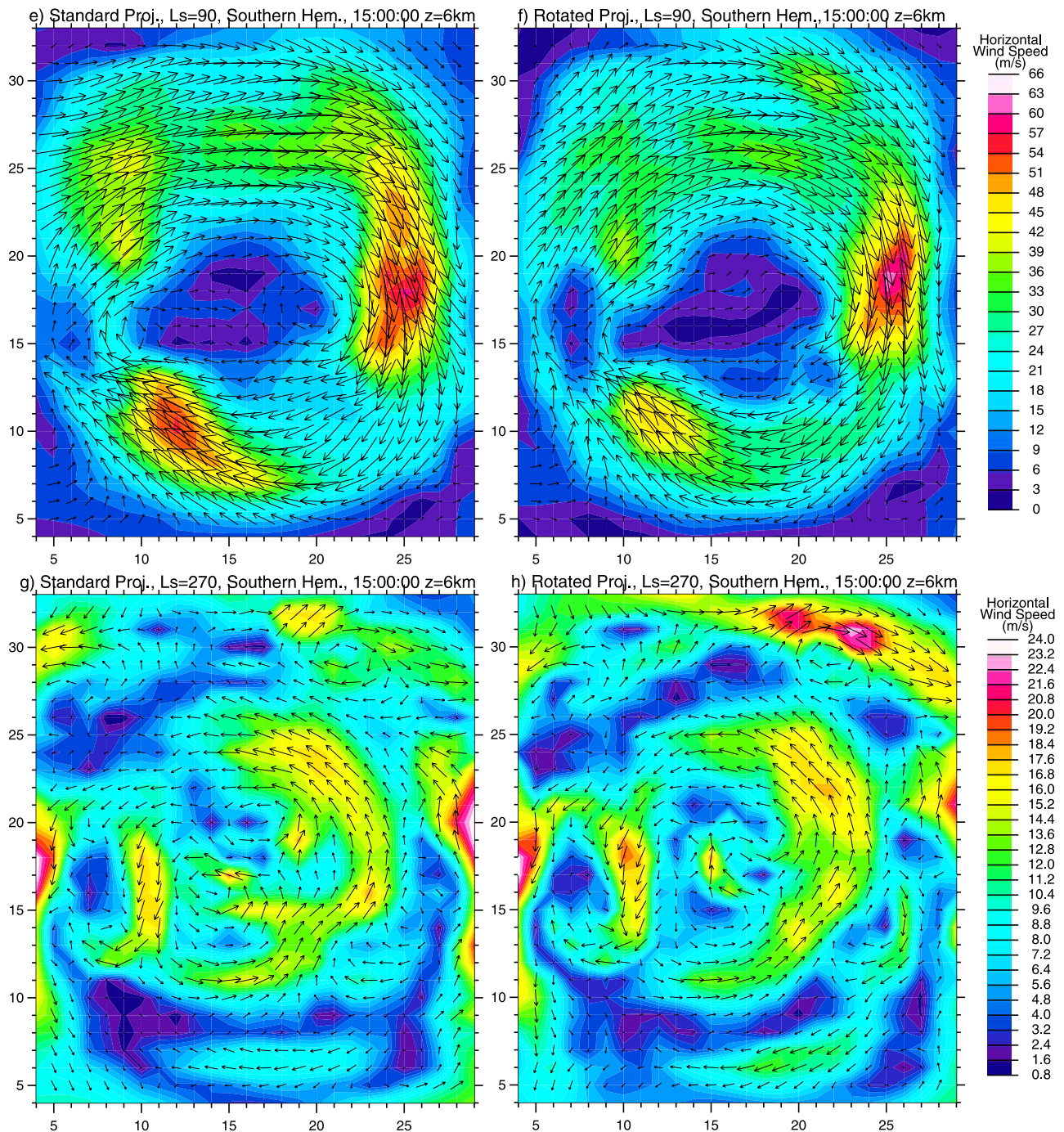


Figure 13. (continued)

[55] Advecting haze particles and radiatively active gases within the model atmosphere will affect these temperature gradients by affecting the spatial distribution of heating and cooling, possibly producing a better match to observations [e.g., Tokano *et al.*, 1999; Lebonnois *et al.*, 2003; Rannou *et al.*, 2004]. Haze advection is currently being included in TitanWRF. Interestingly, TitanWRF does produce the observed upper stratospheric warming over the winter pole (Figure 16d) [Achterberg *et al.*, 2006], probably due to adiabatic heating within the strongly downwelling branch of the solstitial Hadley cell. We will investigate this in the future using a higher model top (currently the top is at

0.2 Pa, but we ignore model results within the damping region that extends down to 2 Pa).

[56] As in midlatitudes, the equatorial zonal winds produced in TitanWRF (peaking at $\sim 13\text{ m/s}$ at a few hundred Pa) are also weaker than observed (e.g., winds exceeding 100 m/s were experienced by the Huygens probe at $\sim 10^\circ\text{S}$ [Folkner *et al.*, 2006]). However, according to Hide's theorem [Hide, 1969; Schneider and Lindzen, 1977], the presence of even weak equatorial superrotation requires upgradient angular momentum transports. For slowly rotating atmospheres such as Titan and Venus, this transport may be accomplished by eddies produced via barotropic

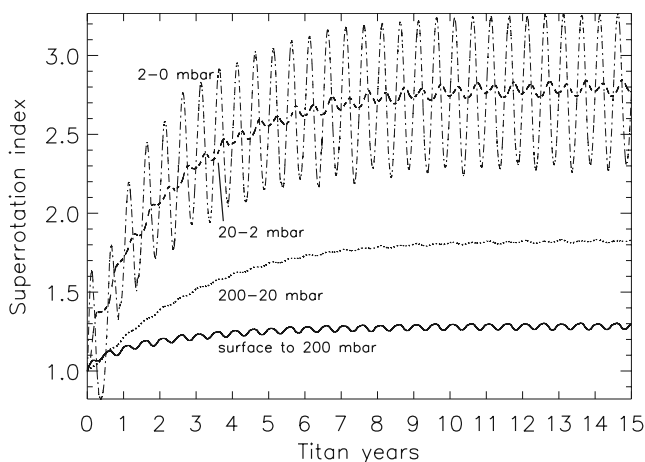


Figure 14. Globally averaged, mass-weighted superrotation index (see text) in four atmospheric layers over 15 Titan years for a TitanWRF simulation started from rest.

instability on the equatorward flanks of midlatitude jets [Gierasch, 1975; Rossow and Williams, 1979]. A necessary condition for barotropic instability is that the northward gradient of vorticity changes sign somewhere in the domain. The shading in Figures 16e and 16f shows $\Gamma = d^2u/dy^2 - \beta$, where u is the zonal-mean zonal wind, y is northward distance and β is df/dy , where f is the Coriolis parameter. The thin contours show zonal-mean zonal wind, and the thick contour line marks where Γ is zero, clearly showing

that likely regions of barotropic instability and wave production exist just equatorward of the zonal jet peaks. We are currently analyzing eddies and angular momentum fluxes produced by the TitanWRF simulations, and will present further details in a future TitanWRF paper.

[57] Figure 17 shows zonal-mean surface temperature versus latitude for the final year of the simulation (year 15). The equator to pole variation and the lag between peak surface temperatures and solar insolation is dependent on the surface properties used. For this simulation we used a thermal inertia of $335 \text{ J m}^{-2} \text{ s}^{-1/2} \text{ K}^{-1}$, an albedo of 0.32 and a surface emissivity of 0.86 (similar to those used for a “porous icy regolith” surface type by Tokano [2005]), but these properties will be varied in simulations restarted from the final (spun up) year of this simulation to assess their effect. The results are quite similar to those shown in Figure 1 of Tokano [2005]. Our minimum polar temperatures occur 30 to 45 degrees of L_s after winter solstice, and the annual temperature variation varies between 1.1 K at the equator and 4.2 K at the south pole (where peak temperatures are higher than at the north pole due to perihelion occurring at $L_s = 281^\circ$, shortly after summer solstice).

6.3. VenusWRF

[58] Initial work with the VenusWRF GCM has involved the simulation of the global circulation, with a focus on understanding superrotation. The VenusWRF GCM uses linearized forcing and dissipation schemes similar to those used for the Held-Suarez comparison described in section 4.2 (but in this case using Venus-like relaxation temperature

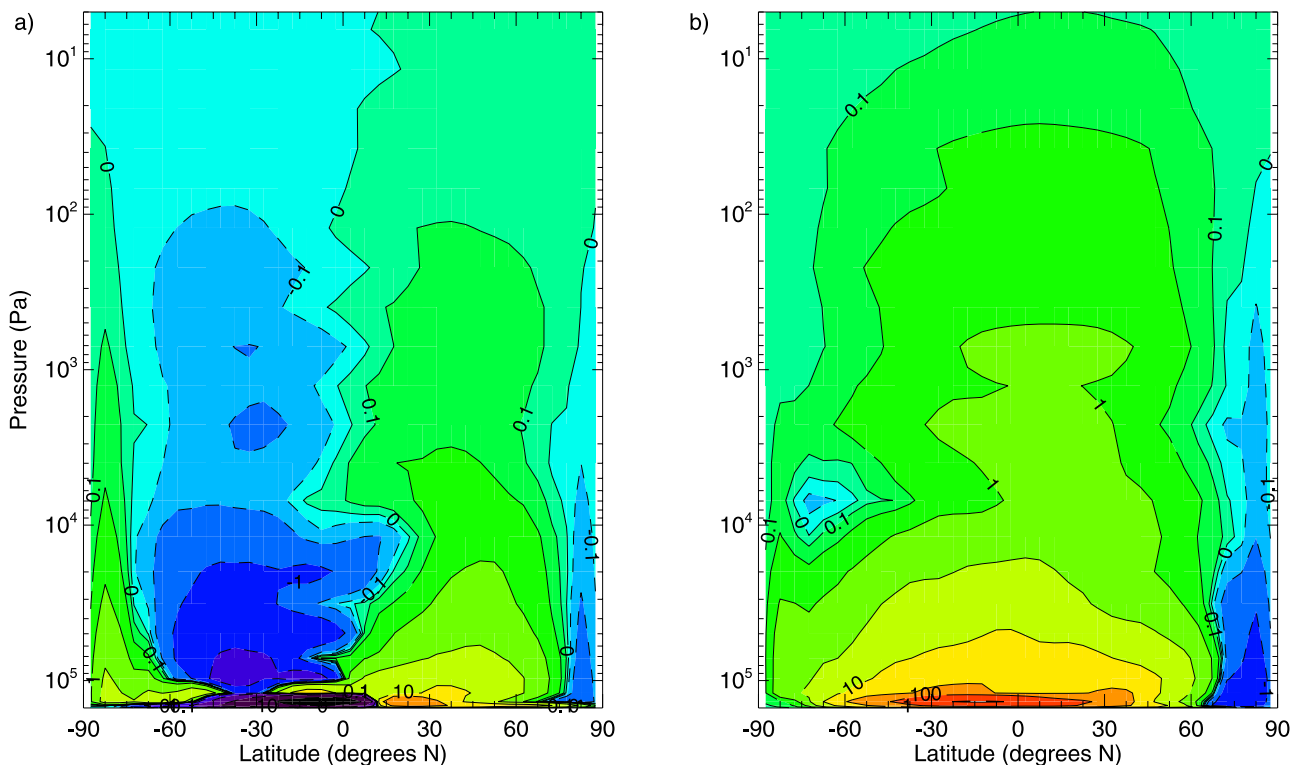


Figure 15. Mass stream function ($1e8 \text{ kg/s}$) averaged over 10 Titan days for (a) northern spring equinox ($L_s = 0^\circ$) and (b) northern summer solstice ($L_s = 90^\circ$) for the TitanWRF simulation. Negative values indicate counterclockwise circulation.

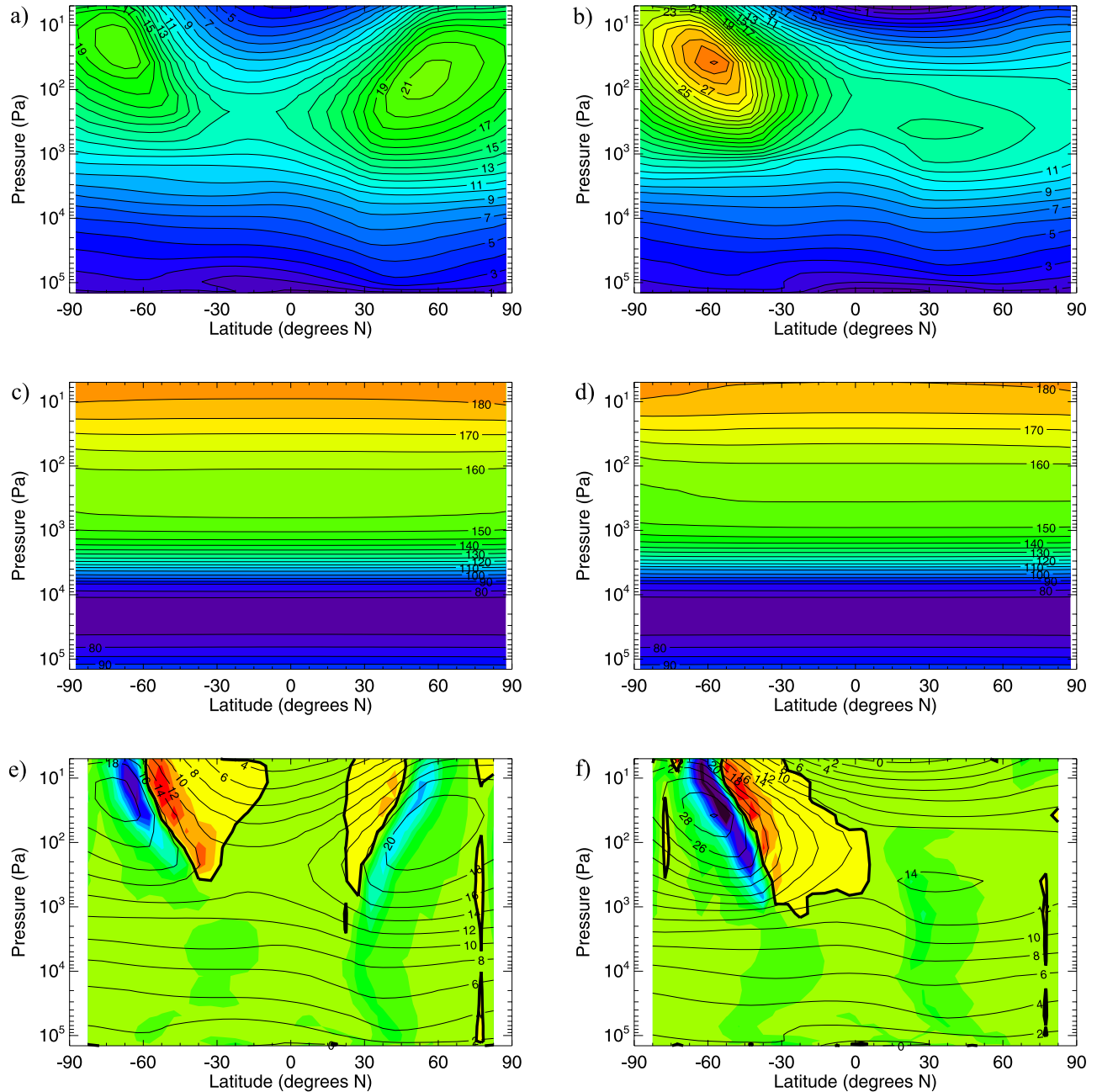


Figure 16. Top row: zonal-mean zonal wind (m/s) averaged over 10 Titan days for (a) $L_s = 24^\circ$, a time of weak hemispheric asymmetry, and (b) $L_s = 65^\circ$, a time of strong hemispheric asymmetry, for the TitanWRF simulation. Middle row: zonal-mean temperatures (K) for (c) $L_s = 24^\circ$ and (d) $L_s = 65^\circ$. Bottom row: thin contours show zonal-mean zonal winds (m/s) for (e) $L_s = 24^\circ$ and (f) $L_s = 65^\circ$. Shading indicates $d^2u/dy^2 - \beta$ (see text), and the thick solid contour shows where this is zero.

profiles and appropriate timescales). In order to assess the model in comparison with other Venus GCMs, preliminary simulations have used the same thermal forcing, relaxation timescales, and damping timescales as applied in the Venus version of the UKMO model [Lee *et al.*, 2005, 2006]. We also used the same vertical levels (with a maximum grid spacing of 3.5 km) and a 36×64 horizontal grid. We have not included a diurnal cycle (thus thermal tides are precluded), and this allows us to ignore the fact that Venus rotates in a retrograde sense (as the relative direction of the

Sun's motion is not relevant). No changes to the model dynamics or forcing are thus required for Venus, as we simply interpret positive zonal winds as westward (i.e., as being in the same sense as the planet's rotation).

[59] Figure 18 shows the horizontal wind components and the temperature field averaged over solar days 34–60 (with the upper atmosphere near equilibrium by the start of this averaging period). The model exhibits westward (positive zonal) winds (Figure 18a) at all levels except at the equatorial surface, and a strong equatorial superrotation at

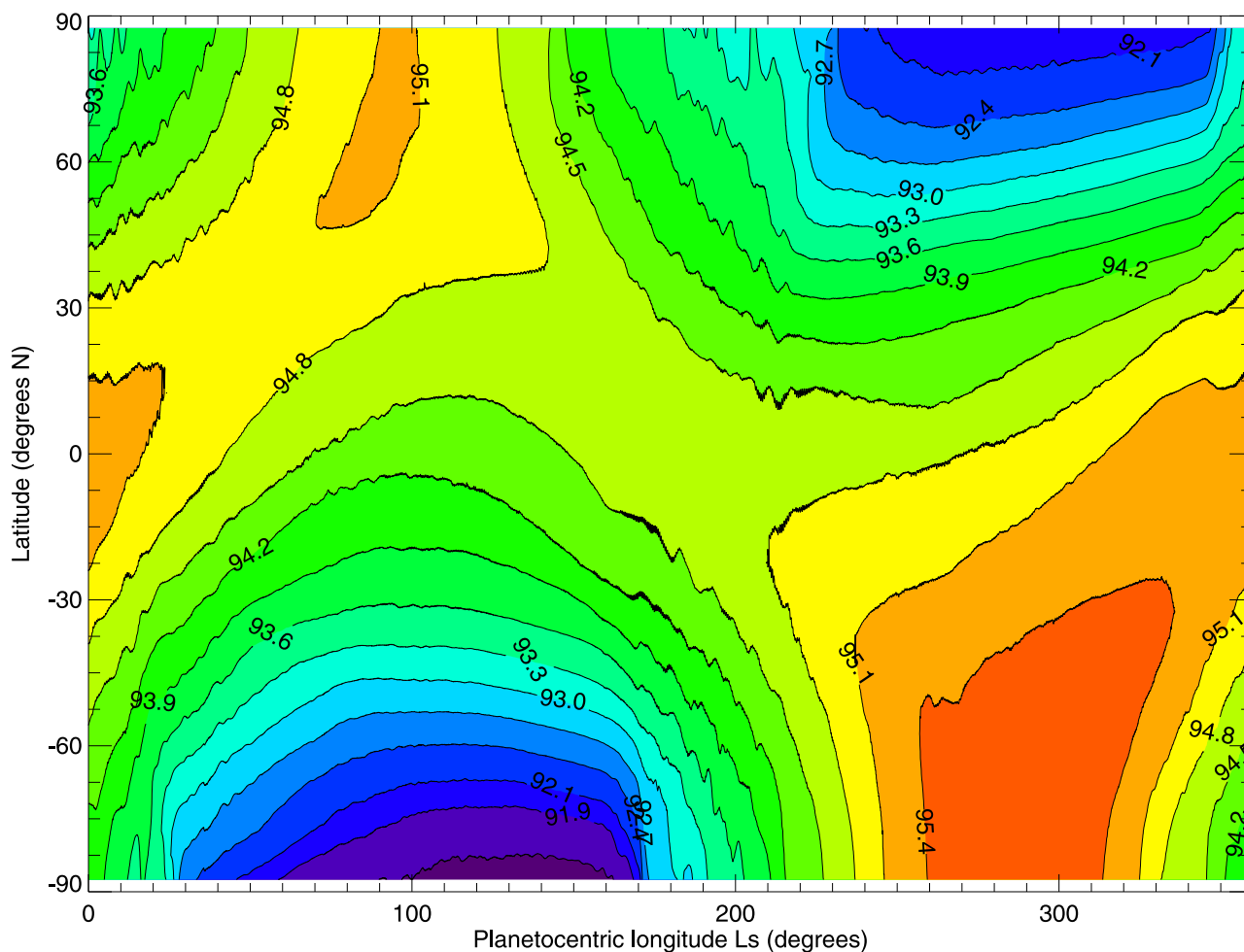


Figure 17. Zonal-mean surface temperatures (in K) throughout year 15 of the TitanWRF simulation.

1 kPa (70 km altitude). The meridional wind field and anomaly temperatures (Figures 18b and 18d, respectively, where anomaly temperature is the zonal mean minus the layer mean temperature) show a single large Hadley cell in the middle atmosphere and a smaller meridional cell near the surface. Both meridional cells are driven by the latitudinal temperature gradient in the prescribed forcing. The spin-up of VenusWRF’s superrotation is much faster than for TitanWRF, with the model reaching a statistically steady state after about 15 years (3500 Earth days). This is because the forcing used [Lee *et al.*, 2006] has an artificially short relaxation timescale to accelerate the spin-up process.

[60] As in the Lee *et al.* [2005] and Yamamoto and Takahashi [2003a, 2003b, 2004] Venus GCMs, the midlatitude jets are barotropically unstable, generating midlatitude waves that transport westward momentum toward the equator to maintain superrotating winds there. There is also a reversal of the meridional temperature gradient in the upper atmosphere (at 100 Pa), which appears as the “warm pole” feature observed by Pioneer Venus [Taylor *et al.*, 1983]. In comparison with Lee *et al.* [2005], however, the peak zonal winds and latitudinal temperature gradients are much larger. This is due to a difference in the dynamical core, specifically the type of horizontal diffusion scheme applied in

VenusWRF. For both VenusWRF and TitanWRF we used the Smagorinsky diffusion scheme on 2-D surfaces (see section 3.4.4), but more scale-selective (∇^6) diffusion was used in the previous Venus work by Lee *et al.* [2005, 2006] and does seem to significantly affect results. We are currently implementing ∇^6 diffusion within WRF, and will discuss this further in future Titan and Venus papers.

7. Summary

[61] This paper is designed to provide a peer-reviewed literature reference for the planetary model derived from the NCAR Weather Research and Forecasting (WRF) model. The main work described in this paper has involved the conversion of the dynamical core for global application and the conversion of the physics drivers and constants for planetary application. The Appendices provide a detailed mathematical description of the specific changes to the dynamical core. This paper also provides characterization and “validation” of the global dynamical core through use of standard forcing scenarios. Detailed planetary validation will be discussed in future papers, but sufficient results are shown to demonstrate that the model works plausibly well in application at various scales to Mars, and at global scales to Titan and Venus.

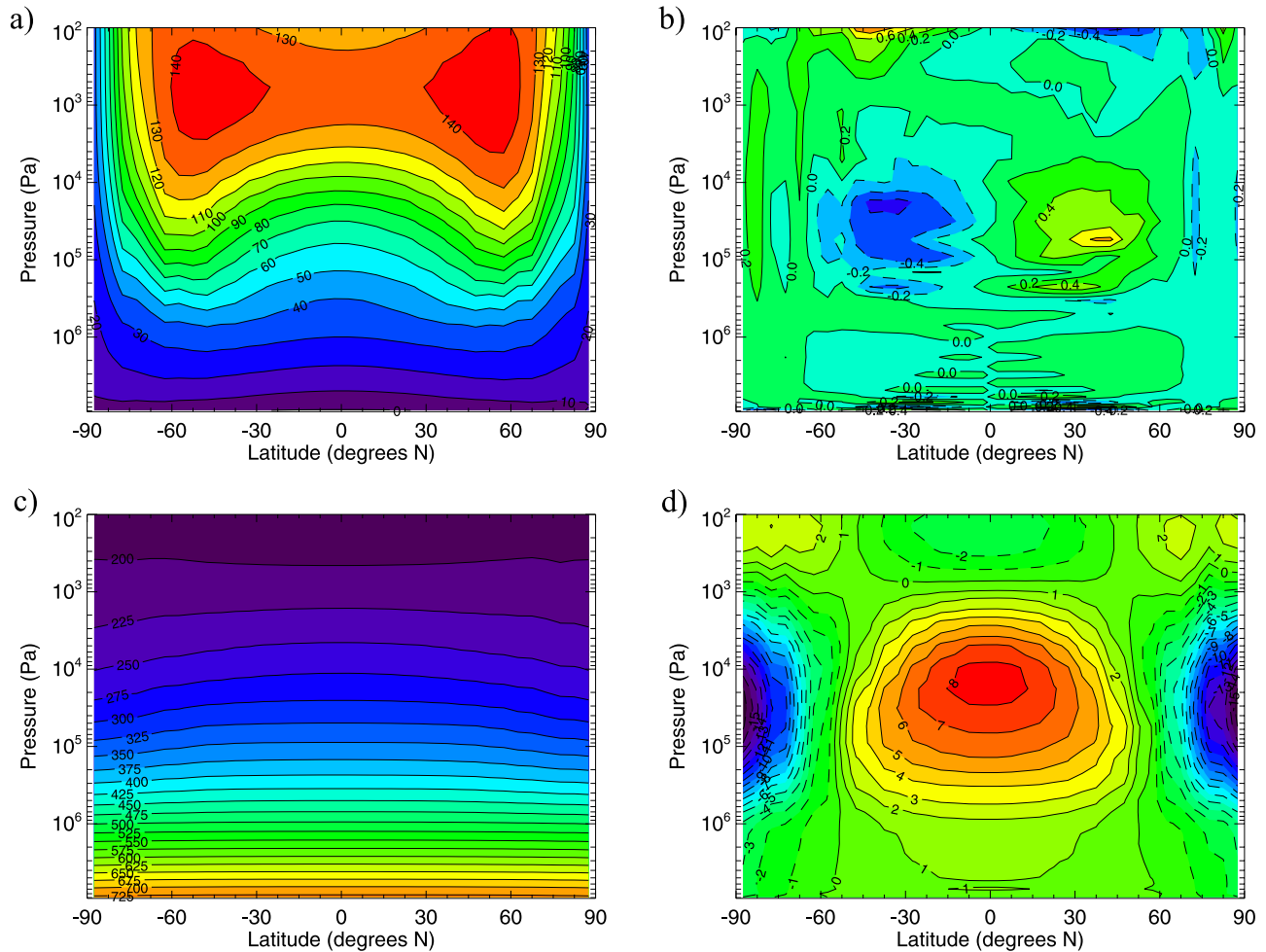


Figure 18. (a) Zonal-mean zonal wind, (b) zonal-mean meridional wind, (c) zonal-mean temperature, and (d) temperature anomaly (the zonal mean minus the layer mean temperature), averaged over solar days 34–60 of the VenusWRF simulation. Positive winds denote westward winds, i.e., winds traveling in the same sense as the planetary rotation (which is retrograde for Venus).

[62] In addition to the results presented in this paper, the Martian WRF GCM has been compared against previously published Martian GCMs by *Wilson et al.* [2006]. The model was found to compare well against the GFDL [*Wilson and Hamilton*, 1996] and LMD [*Forget et al.*, 1999] models in particular. The comparisons extended to the zonal-mean temperature and zonal wind fields, the thermotidal components, and the strength of the mean meridional overturning. This intercomparison suggests that the planetWRF model in Mars GCM mode performs as well in an overall sense as the best of the current global Martian models.

[63] Our tests in this paper demonstrate that the model can reproduce previous model results to the state of the art in the following respects: (1) zonal mean and eddy behavior using the *Held and Suarez* [1994] simplified forcing, (2) long-term (decadal) mean mass and angular momentum conservation of much better than 0.01% and 0.1%, respectively, for the HS94 forcing, (3) wave and tracer propagation in the presence of a polar boundary condition and filtering, (4) scales of thermal convection in the Martian daytime boundary layer, (5) magnitude of thermally driven slope winds on the walls of Valles Marineris, (6) zonal-mean temperature and zonal winds for the Martian atmo-

sphere at multiple resolutions and with differing location of the computational pole, and (7) spin-up of a superrotating atmosphere for Titan and Venus.

Appendix A: Flux Form of the Fluid Dynamic Conservation Equations, Including Two-Dimensional and Two-Directional Map Scale Factors

[64] Here we present the fluid dynamical equations solved in our model, written with the use of two directional (i.e., not conformal) map scale factors. First, let

- X, Y, Z = curvilinear Earth coordinates: X , positive eastward; Y , positive northward; Z , positive upward
- x, y, z = map coordinates (projected system)
- U, V, W = velocity components relative to Earth along the X, Y, Z directions
- u, v, w = velocity components relative to Earth along the x, y, z directions

[65] For a generalized (but orthogonal) map projection where $x = f(X)$ and $y = g(Y)$ only (i.e., no rotation of axes), we can define the metric coefficients as

$$\begin{aligned} dX &= h_x dx \\ dY &= h_y dy \end{aligned}$$

where

$$\begin{aligned} h_x &\equiv \frac{\partial f}{\partial x} = \frac{1}{m_x} \\ h_y &\equiv \frac{\partial g}{\partial y} = \frac{1}{m_y} \end{aligned}$$

[66] The map projection only affects the horizontal derivatives, and the horizontal derivatives in the two coordinate systems are related by

$$\begin{aligned} \frac{\partial}{\partial X} &\equiv \frac{1}{h_x} \frac{\partial}{\partial x} = m_x \frac{\partial}{\partial x} \\ \frac{\partial}{\partial Y} &\equiv \frac{1}{h_y} \frac{\partial}{\partial y} = m_y \frac{\partial}{\partial y} \end{aligned}$$

[67] Since there is no rotation of axes,

$$\begin{aligned} u &= U \\ v &= V \end{aligned}$$

[68] Next, we convert the complete set of conservation equations (heat, momentum, mass):

$$\begin{aligned} \frac{DT}{Dt} &= F_q \\ \frac{DU}{Dt} &= -\frac{1}{\rho} \frac{\partial P}{\partial x} + F_x \\ \frac{DV}{Dt} &= -\frac{1}{\rho} \frac{\partial P}{\partial y} + F_y \\ \frac{DW}{Dt} &= -\frac{1}{\rho} \frac{\partial P}{\partial z} + F_z \\ \frac{D\rho}{Dt} &= \rho \bar{\nabla} \cdot \bar{V} \end{aligned}$$

[69] Here, T is temperature, P is pressure, ρ is density, $\bar{V} \equiv U\hat{i} + V\hat{j} + W\hat{k}$, the various F 's are forcing terms (includes planetary curvature and the full three-dimensional Coriolis effect for the momentum equations), and the definition of the advective derivative is

$$\frac{D}{Dt} \equiv \frac{\partial}{\partial t} + U \frac{\partial}{\partial X} + V \frac{\partial}{\partial Y} + W \frac{\partial}{\partial Z}$$

[70] The energy conservation equation only involves horizontal derivatives in its advective derivative term, and the forcing terms generally do not include horizontal derivatives, with the exception of inclusion of a diffusive term.

Since the energy equation is the simplest with respect to map scale factors, we can cast it in the following form using all of our above definitions (particularly the equivalence of \bar{v} and \bar{V}):

$$\frac{\partial T}{\partial t} = -m_x u \frac{\partial T}{\partial x} - m_y v \frac{\partial T}{\partial y} - w \frac{\partial T}{\partial z} + F_q$$

[71] The definition of divergence in a ‘‘horizontally stretched’’ Cartesian grid (e.g., a map projection, such as we are interested in here) is [e.g., *Haltiner and Williams*, 1980]

$$\bar{\nabla} \cdot \bar{A} = m_x m_y \left[\frac{\partial}{\partial x} \left(\frac{A_x}{m_y} \right) + \frac{\partial}{\partial y} \left(\frac{A_y}{m_x} \right) \right] + \frac{\partial A_z}{\partial z}$$

and so the mass conservation equation can be quickly rewritten as (after combining a few advective derivative terms with similar terms on the right-hand side of the equation)

$$\frac{\partial \rho}{\partial t} = -m_x m_y \left[\frac{\partial}{\partial X} \left(\frac{\rho u}{m_y} \right) + \frac{\partial}{\partial Y} \left(\frac{\rho v}{m_x} \right) \right] + \frac{\partial}{\partial Z} (\rho w)$$

[72] Finally, the momentum equations are recast as

$$\begin{aligned} \frac{\partial u}{\partial t} &= -m_x u \frac{\partial u}{\partial x} - m_y v \frac{\partial u}{\partial y} - w \frac{\partial u}{\partial z} - m_x \frac{1}{\rho} \frac{\partial P}{\partial x} + F_x \\ \frac{\partial v}{\partial t} &= -m_x u \frac{\partial v}{\partial x} - m_y v \frac{\partial v}{\partial y} - w \frac{\partial v}{\partial z} - m_y \frac{1}{\rho} \frac{\partial P}{\partial y} + F_y \\ \frac{\partial w}{\partial t} &= -m_x u \frac{\partial w}{\partial x} - m_y v \frac{\partial w}{\partial y} - w \frac{\partial w}{\partial z} - \frac{1}{\rho} \frac{\partial P}{\partial z} + F_z \end{aligned}$$

[73] To improve model conservation, the equations solved in the model are cast in a flux form. That is, the tendencies of temperature, momentum components, and moisture variables (as well as other minor atmospheric components, aerosol or gas) are solved for with those respective terms multiplied by density (in the older ‘‘height coordinate’’ version of WRF) or by total column mass (in the newer ‘‘mass coordinate’’ version of WRF). For simplicity, we here show the flux form of the equations coupled with density. The mass conservation equation is already a flux equation, and thus is unmodified internally in the model. The flux form of the equations can be derived by multiplying the mass conservation equation by the appropriate term (T , u , v , or w), multiplying the corresponding equation for the appropriate term by ρ , and then adding the two together and simplifying the terms. In the case of temperature, the final flux form of the equation becomes

$$\begin{aligned} \frac{\partial}{\partial t} (\rho T) &= -m_x m_y \frac{\partial}{\partial x} \left(\frac{\rho u}{m_y} T \right) - m_x m_y \frac{\partial}{\partial y} \left(\frac{\rho v}{m_x} T \right) - \frac{\partial}{\partial z} (\rho w T) \\ &\quad + \rho F_q \end{aligned}$$

[74] The momentum equations become

$$\begin{aligned}\frac{\partial}{\partial t} \left(\frac{\rho u}{m_y} \right) &= -m_x \frac{\partial}{\partial x} \left(\frac{\rho u}{m_y} u \right) - m_x \frac{\partial}{\partial y} \left(\frac{\rho v}{m_x} u \right) \\ &\quad - \frac{1}{m_y} \frac{\partial}{\partial z} (\rho w u) - \frac{m_x}{m_y} \frac{\partial P}{\partial x} + \frac{\rho}{m_y} F_x \\ \frac{\partial}{\partial t} \left(\frac{\rho v}{m_x} \right) &= -m_y \frac{\partial}{\partial x} \left(\frac{\rho u}{m_y} v \right) - m_y \frac{\partial}{\partial y} \left(\frac{\rho v}{m_x} v \right) \\ &\quad - \frac{1}{m_x} \frac{\partial}{\partial z} (\rho w v) - \frac{m_y}{m_x} \frac{\partial P}{\partial y} + \frac{\rho}{m_x} F_y \\ \frac{\partial}{\partial t} (\rho w) &= -m_x m_y \frac{\partial}{\partial x} \left(\frac{\rho u}{m_y} w \right) - m_x m_y \frac{\partial}{\partial y} \left(\frac{\rho v}{m_x} w \right) \\ &\quad - \frac{\partial}{\partial z} (\rho w w) - \frac{\partial P}{\partial z} + \rho F_z\end{aligned}$$

[75] The moisture conservation equations are the same as the energy flux equation above, with the variable T simply replaced by the appropriate moisture mass mixing ratio variable.

[76] For the simple cylindrical (or Plate Carrée) map projection commonly used (by us as well) for global simulations, the following definitions are used:

$$\begin{aligned}x &= a\lambda \\ y &= a\phi \\ dx &= a d\lambda \\ dy &= a d\phi \\ dX &= a \cos \phi d\lambda \\ dY &= a d\phi \\ m_x &= \sec \phi \\ m_y &= 1\end{aligned}$$

with the usual definitions of ϕ = latitude (radians), λ = longitude (radians), and a = radius of the planet. The values of map scale factors in the x and y directions are precomputed, stored as arrays, and used as appropriate when numerically integrating the full set of equations. The simple cylindrical projection, as its name implies, is a simple case, but the method is completely general and thus more complicated map projections could easily be added, as long as the functional form of the map scale factors is known or derivable.

Appendix B: Fourier Filtering of Field Variables Near the Map Projection Poles

[77] In general, a larger physical distance between model grid points allows a longer time step to be used (see main text, section 3.2). In a global domain version of WRF,

however, the east-west separation decreases toward the poles, as points spaced equally in longitude become closer together in real space. These grid points thus determine how large the time step can be before breaking the CFL criterion. In order to allow for longer time steps (and thus more effective use of computer resources), a typical approach is to one-dimensionally Fourier filter the dynamical fields near the pole along the east-west direction. This implies Fourier transforming some variable (but only in the east-west direction), applying a filter on the transform, and then inverse transforming this back to grid-box space. The filtering typically removes high-frequency information, creating a “virtual grid box size” that is larger than the actual grid box size, and thus preventing CFL violations from occurring as easily.

[78] We allow three options for our Fourier filter, all of which are derived from the literature. Two apply a cutoff frequency to the transformed fields, essentially acting as low-pass filters, where the cutoff frequency is a function of distance from the pole (i.e., latitude). The third is both a low-pass and a high-pass filter, while damping out the medium frequencies, what we call an “anti-medium-pass filter.” Again, the form of the function and which frequencies are allowed to pass any or all of their power through is a function of latitude. In all cases, the latitudinal dependence arises because the width of the grid box in physical space increases as the grid box moves away from the pole, and thus filtering becomes less necessary. Since filtering removes information from the data, the desire to extend the time step must be balanced by the desire to maintain sufficient information at high latitudes.

B1. Low-Pass Cutoff Filtering

[79] In two of the cases used for Fourier filtering, simple low-pass cutoff filtering is performed on the Fourier transformed data. In the first case, the cutoff frequency (actually, wave number, κ) is defined by the following function:

$$\kappa_{\max} = (N/2) \cos \phi, \quad |\phi| > 60^\circ$$

where N is the number of points in the x direction, and ϕ is latitude. All wave numbers lower than this value have 100% of their power preserved, while all wave numbers higher than this value have their power set to 0. The second case using a low-pass filtering method uses a predetermined list of the maximum wave number to be retained at each latitude.

B2. Anti-Medium-Pass Filtering

[80] In the other type of filtering we have implemented, the filter function is a sort of an “anti-medium-pass” filter in that it acts as both a low- and high-pass filter, while removing all medium wavelength information. In this case, filtering is only done between 90° and 75° . The functional form of this filter is

$$P(\phi, \nu) = \cos \phi / [\cos(\pi/4) \sin^4 \nu], \quad |\phi| > 75^\circ$$

where ν is $\pi\kappa/N$. The value of P at a particular wave number is then multiplied by the complex value of the Fourier transform at that wave number.

Appendix C: Rotated Pole (Transverse Projection)

[81] In the standard definition of the cylindrical projection (the “simple,” or “Plate Carrée”), the surface of the sphere is cut along a meridian of longitude (either 180° or 0°) from north to south pole, and the two poles are “stretched” to make a line. But there is nothing intrinsic in the definition of the simple cylindrical projection that requires the planet’s rotational (north/south) poles to be the mathematical (top/bottom) poles of the projection. One can imagine picking any two antipodal points on the globe and then cutting the surface open along half of the great circle between them. Doing this creates what is called a “transverse” cylindrical projection (as opposed to “simple”). The most famous example of a transverse cylindrical projection is known as the Cassini projection. It should be noted that the transverse projection does not change the computational mesh in any way (for a fixed model resolution, the physical distance between any two grid points, and the shape and size of the mesh, is the same regardless of the mesh orientation); all that is affected is the actual geographical location of the computational grid points. (The transverse grid can sometimes be difficult to visualize, as per a comment by one of our reviewers. The best way that we have to visualize it is to imagine making a wire mesh corresponding to the computational model latitudinal and longitudinal grid lines. Now imagine placing this spherical mesh or cage loosely over a ball. It should be immediately obvious that by placing one’s fingers on the mesh poles (the two places where the wires converge), one can rotate the mesh relative to the ball without distorting either.)

[82] In the simple cylindrical projection, the north pole (90°N latitude, all longitudes) is at the top, and the south pole (90°S latitude, all longitudes) is at the bottom. The left and right edges are the longitudes -180° and $+180^\circ$, respectively. In the Cassini version of the transverse cylindrical projection, the “north pole” of the projection is now at 0°E (all latitudes), and the “south pole” is at 180°E (all latitudes). The left and right edges are the equator (0°N) between the longitudes of 0°E and 180°E .

[83] The equations that describe the transformation of coordinates from actual, geographical latitude and longitude (Φ, Λ) to projected or “computational” latitude and longitude (ϕ, λ) are presented in this appendix [see also *Suarez and Takacs, 1995*]. Three extra parameters are needed in these equations, and they are: (ϕ_{NP}, λ_{NP}), which describe the location of the geographical (true, rotational) north pole in the projected (or computational) coordinates, and λ_0 , which is a measure of the rotation around the geographical pole.

$$\begin{aligned}\sin \phi &= \cos \phi_{NP} \cos \Phi \cos(\Lambda + \lambda_0 - \pi) \\ &\quad + \sin \phi_{NP} \sin \Phi \\ \cos(\lambda + \pi - \lambda_{NP}) \cos \phi &= \sin \phi_{NP} \cos \Phi \cos(\Lambda + \lambda_0 - \pi) \\ &\quad - \cos \phi_{NP} \sin \Phi \\ \sin(\lambda + \pi - \lambda_{NP}) \cos \phi &= \cos \Phi \sin(\Lambda + \lambda_0 - \pi)\end{aligned}$$

[84] The inverse equations to convert from projected latitude and longitude back to geographical latitude and longitude are

$$\begin{aligned}\sin \Phi &= \cos \phi_{NP} \cos \phi \cos(\lambda - \lambda_{NP}) \\ &\quad + \sin \phi_{NP} \sin \phi \\ \cos(\Lambda + \lambda_0) \cos \Phi &= \sin \phi_{NP} \cos \phi \cos(\lambda - \lambda_{NP}) \\ &\quad - \cos \phi_{NP} \sin \phi \\ \sin(\Lambda + \lambda_0) \cos \Phi &= \cos \phi \sin(\lambda - \lambda_{NP})\end{aligned}$$

[85] The two sets of equations are related. One can create the other by making the transformations

$$\begin{aligned}(\phi, \lambda) &\iff (\Phi, \Lambda) \\ \lambda_{NP} &\iff \pi - \lambda_0\end{aligned}$$

[86] Only the Coriolis parameter needs to be changed when using these newly rotated coordinates, and is now written as

$$f = 2\Omega \sin \Phi = 2\Omega(\cos \phi_{NP} \cos \phi \cos(\lambda - \lambda_{NP}) + \sin \phi_{NP} \sin \phi)$$

[87] Last, we need to obtain U and V , the true east-west and north-south winds, respectively, for examining model output, etc. To convert between these and u and v (winds in the left-right and top-bottom directions, respectively, in our projection), we use

$$\begin{aligned}\cos \Phi \cos \alpha &= \sin \phi_{NP} \cos \phi - \cos(\lambda - \lambda_{NP}) \cos \phi_{NP} \sin \phi \\ \cos \Phi \sin \alpha &= \sin(\lambda - \lambda_{NP}) \cos \phi_{NP}\end{aligned}$$

where α , the local angle between the computational and geographical coordinates, is calculated from

$$\begin{aligned}u &= U \cos \alpha - V \sin \alpha \\ v &= U \sin \alpha + V \cos \alpha \\ U &= v \sin \alpha + u \cos \alpha \\ V &= v \cos \alpha - u \sin \alpha\end{aligned}$$

[88] **Acknowledgments.** We wish to thank Chris McKay for providing the latest version of the *McKay et al. [1989]* Titan radiative transfer code, Chris Lee for implementing the VenusWRF physical parameterizations and for Figure 18, and Shawn Ewald for unrotating the “rotated pole” results and rotating the “standard” results in Figures 11, 12, and 13. We also wish to thank Bill Skamarock, Joe Klemp, Jimi Dudhia, John Michalakes, and the rest of the WRF Development Teams at NCAR for their invaluable help and advice, and to thank our reviewers for their useful comments and suggestions. The majority of this work was funded through NASA’s AISR program, with funding for TitanWRF development coming from NASA’s OPR program. The simulations presented in this paper were performed on Caltech’s Division of Geological and Planetary Sciences Dell cluster.

References

Achterberg, R. K., B. J. Conrath, P. J. Gierasch, F. M. Flasar, and C. A. Nixon (2006), Thermal structure of Titan’s stratosphere from Cassini

- CIRS limb observations, paper presented at 38th Annual Division for Planetary Sciences Meeting, Am. Astron. Soc., Pasadena, Calif.
- Arakawa, A., and V. R. Lamb (1977), Computational design of the basic dynamical processes of the UCLA general circulation model, *Methods Comput. Phys.*, *17*, 173–265.
- Basu, S., M. I. Richardson, and R. J. Wilson (2004), Simulation of the Martian dust cycle with the GFDL Mars GCM, *J. Geophys. Res.*, *109*, E11006, doi:10.1029/2004JE002243.
- Chen, M. H., R. B. Rood, and L. L. Takacs (1997), Impact of a semi-Lagrangian and an Eulerian dynamical core on climate simulations, *J. Clim.*, *10*(9), 2374–2389.
- Dowling, T. E., A. S. Fischer, P. J. Gierasch, J. Harrington, R. P. LeBeau, and C. M. Santori (1998), The explicit planetary isentropic-coordinate (EPIC) atmospheric model, *Icarus*, *132*(2), 221–238.
- Dowling, T. E., et al. (2006), The EPIC atmospheric model with an isentropic/terrain-following hybrid vertical coordinate, *Icarus*, *182*(1), 259–273.
- Flasar, F. M., et al. (2005), Titan's atmospheric temperatures, winds, and composition, *Science*, *308*, 975–978.
- Folkner, W. M., et al. (2006), Winds on Titan from ground-based tracking of the Huygens probe, *J. Geophys. Res.*, *111*, E07S02, doi:10.1029/2005JE002649.
- Forget, F., F. Hourdin, R. Fournier, C. Hourdin, O. Talagrand, M. Collins, S. R. Lewis, P. L. Read, and J. P. Huot (1999), Improved general circulation models of the Martian atmosphere from the surface to above 80 km, *J. Geophys. Res.*, *104*(E10), 24,155–24,175.
- Fox-Rabinovitz, M. S., G. L. Stenchikov, M. J. Suarez, and L. L. Takacs (1997), A finite-difference GCM dynamical core with a variable-resolution stretched grid, *Mon. Weather Rev.*, *125*(11), 2943–2968.
- Fox-Rabinovitz, M. S., G. L. Stenchikov, M. J. Suarez, L. L. Takacs, and R. C. Govindaraju (2000), A uniform- and variable-resolution stretched-grid GCM dynamical core with realistic orography, *Mon. Weather Rev.*, *128*(6), 1883–1898.
- Gierasch, P. J. (1975), Meridional circulation and the maintenance of the Venus atmospheric rotation, *J. Atmos. Sci.*, *32*, 1038–1044.
- Haberle, R. M., H. C. Houben, R. Hertenstein, and T. Herdtle (1993a), A boundary-layer model for Mars—Comparison with Viking lander and entry data, *J. Atmos. Sci.*, *50*, 1544–1559.
- Haberle, R. M., J. B. Pollack, J. R. Barnes, R. W. Zurek, C. B. Leovy, J. R. Murphy, H. Lee, and J. Schaeffer (1993b), Mars atmospheric dynamics as simulated by the NASA Ames general circulation model: 1. The zonal-mean circulation, *J. Geophys. Res.*, *98*(E2), 3093–3123.
- Haberle, R. M., M. M. Joshi, J. R. Murphy, J. R. Barnes, J. T. Schofield, G. Wilson, M. Lopez-Valverde, J. L. Hollingsworth, A. F. C. Bridger, and J. Schaeffer (1999), General circulation model simulations of the Mars Pathfinder atmospheric structure investigation/meteorology data, *J. Geophys. Res.*, *104*(E4), 8957–8974.
- Haberle, R. A., J. R. Murphy, and J. Schaeffer (2003), Orbital change experiments with a Mars general circulation model, *Icarus*, *161*(1), 66–89.
- Haltiner, G. J., and R. T. Williams (1980), *Numerical Prediction and Dynamic Meteorology*, 2nd ed., John Wiley, New York.
- Hartogh, P., A. S. Medvedev, T. Kuroda, R. Saito, G. Villanueva, A. G. Feofilov, A. A. Kutepov, and U. Berger (2005), Description and climatology of a new general circulation model of the Martian atmosphere, *J. Geophys. Res.*, *110*, E11008, doi:10.1029/2005JE002498.
- Held, I. M., and M. J. Suarez (1994), A proposal for the intercomparison of the dynamical cores of atmospheric general-circulation models, *Bull. Am. Meteorol. Soc.*, *72*(10), 1825–1830.
- Hide, R. (1969), Dynamics of the atmospheres of the major planets with an appendix on the viscous boundary layer at the rigid bounding surface of an electrically-conducting rotating fluid in the presence of a magnetic field, *J. Atmos. Sci.*, *26*, 841–853.
- Hong, S. Y., and H. L. Pan (1996), Nonlocal boundary layer vertical diffusion in a Medium-Range Forecast Model, *Mon. Weather Rev.*, *124*(10), 2322–2339.
- Hourdin, F., O. Talagrand, R. Sadoury, R. Courtin, D. Gautier, and C. P. McKay (1995), Numerical-simulation of the general-circulation of the atmosphere of Titan, *Icarus*, *117*(2), 358–374.
- Hueso, R., and A. Sánchez-Lavega (2006), Methane storms on Saturn's moon Titan, *Nature*, *442*, 428–431.
- Jacobson, M. Z. (1999), *Fundamentals of Atmospheric Modeling*, Cambridge Univ. Press, Cambridge, U. K.
- Kahn, R. A., T. Z. Martin, R. W. Zurek, and S. W. Lee (1992), The Martian dust cycle, in *Mars*, edited by H. H. Kieffer et al., chap. 29, pp. 1017–1053, Univ. of Ariz. Press, Tucson.
- Kahre, M. A., J. R. Murphy, R. M. Haberle, F. Montmessin, and J. Schaeffer (2005), Simulating the Martian dust cycle with a finite surface dust reservoir, *Geophys. Res. Lett.*, *32*, L20204, doi:10.1029/2005GL023495.
- Kahre, M. A., J. R. Murphy, and R. M. Haberle (2006), Modeling the Martian dust cycle and surface dust reservoirs with the NASA Ames general circulation model, *J. Geophys. Res.*, *111*, E06008, doi:10.1029/2005JE002588.
- Kalnay, E. (2002), *Atmospheric Modeling, Data Assimilation and Predictability*, Cambridge Univ. Press, Cambridge, U. K.
- Khairoutdinov, M., D. Randall, and C. DeMott (2005), Simulations of the atmospheric general circulation using a cloud-resolving model as a super-parameterization of physical processes, *J. Atmos. Sci.*, *62*(7), 2136–2154.
- Kuroda, T., N. Hashimoto, D. Sakai, and M. Takahashi (2005), Simulation of the Martian atmosphere using a CCSR/NIES AGCM, *J. Meteorol. Soc. Jpn.*, *83*(1), 1–19.
- Laprise, R. (1992), The Euler equations of motion with hydrostatic-pressure as an independent variable, *Mon. Weather Rev.*, *120*(1), 197–208.
- Lebonnois, S., F. Hourdin, P. Rannou, D. Luz, and D. Toublanc (2003), Impact of the seasonal variations of composition on the temperature field of Titan's stratosphere, *Icarus*, *163*(1), 164–174.
- Lee, C., S. R. Lewis, and P. L. Read (2005), A numerical model of the atmosphere of Venus, *Adv. Space Res.*, *36*(11), 2142–2145.
- Lee, C., S. R. Lewis, and P. L. Read (2006), Producing and understanding the super-rotation in a simple numerical model of Venus, paper presented at Chapman Conference—Exploring Venus as a Terrestrial Planet, Lunar and Planet. Inst., Key Largo, Fla. (Available at http://www.lpi.usra.edu/vexag/chapman_conf/presentations)
- Lellouch, E., A. Coustenis, D. Gautier, F. Raulin, N. Dubouloz, and C. Frere (1989), Titan's atmosphere and hypothesized ocean—A reanalysis of the Voyager-1 radio-occultation and IRIS 7.7 micron data, *Icarus*, *72*(2), 328–349.
- Leovy, C., and Y. Mintz (1969), The numerical simulation of atmospheric circulation and climate of Mars, *J. Atmos. Sci.*, *26*(6), 1167–1190.
- Lewis, S. R., M. Collins, P. L. Read, F. Forget, F. Hourdin, R. Fournier, C. Hourdin, O. Talagrand, and J. P. Huot (1999), A climate database for Mars, *J. Geophys. Res.*, *104*(E10), 24,177–24,194.
- Lin, S. J. (2004), A vertically Lagrangian finite-volume dynamical core for global models, *Mon. Weather Rev.*, *132*(10), 2293–2307.
- Lopez-Valverde, M. A., D. P. Edwards, M. Lopez-Puertas, and C. Roldan (1998), Non-local thermodynamic equilibrium in general circulation models of the Martian atmosphere: 1. Effects of the local thermodynamic equilibrium approximation on thermal cooling and solar heating, *J. Geophys. Res.*, *103*(E7), 16,799–16,811.
- Louis, J. F. (1979), Parametric model of vertical eddy fluxes in the atmosphere, *Boundary Layer Meteorol.*, *17*(2), 187–202.
- Luz, D., F. Hourdin, P. Rannou, and S. Lebonnois (2003), Latitudinal transport by barotropic waves in Titan's stratosphere. II. Results from a coupled dynamics-microphysics-photochemistry GCM, *Icarus*, *166*(2), 343–358.
- Määttänen, A., and H. Savijärvi (2004), Sensitivity tests with a one-dimensional boundary-layer Mars model, *Boundary Layer Meteorol.*, *113*(3), 305–320.
- McKay, C. P., J. B. Pollack, and R. Courtin (1989), The thermal structure of Titan's atmosphere, *Icarus*, *80*(1), 23–53.
- Mellor, G. L., and T. Yamada (1982), Development of a turbulence closure model for geophysical fluid problems, *Rev. Geophys.*, *20*, 851–875.
- Michaels, T. I., and S. C. R. Raffin (2004), Large-eddy simulation of atmospheric convection on Mars, *Q. J. R. Meteorol. Soc.*, *130*(599), 1251–1274.
- Michalakes, J., J. Dudhia, D. Gill, T. Henderson, J. Klemp, W. Skamarock, and W. Wang (2004), The Weather Research and Forecast Model: Software architecture and performance, in *Proceedings of the 11th ECMWF Workshop on the Use of High Performance Computing in Meteorology*, edited by G. Mozdzyński, pp. 156–168, Eur. Cent. for Medium-Range Weather Forecasts, Reading, U.K.
- Moudden, Y., and J. C. McConnell (2005), A new model for multiscale modeling of the Martian atmosphere, GM3, *J. Geophys. Res.*, *110*, E04001, doi:10.1029/2004JE002354.
- Newman, C. E., S. R. Lewis, P. L. Read, and F. Forget (2002a), Modeling the Martian dust cycle: 1. Representations of dust transport processes, *J. Geophys. Res.*, *107*(E12), 5123, doi:10.1029/2002JE001910.
- Newman, C. E., S. R. Lewis, P. L. Read, and F. Forget (2002b), Modeling the Martian dust cycle 2. Multiannual radiatively active dust transport simulations, *J. Geophys. Res.*, *107*(E12), 5124, doi:10.1029/2002JE001920.
- Odaka, M., K. Nakajima, S. Takehiro, M. Ishiwatari, and Y. Y. Hayashi (1998), Numerical study of the Martian atmospheric convection with a two-dimensional anelastic model, *Earth Planets Space*, *50*(5), 431–437.
- Ooyama, K. V. (1990), A thermodynamic foundation for modeling the moist atmosphere, *J. Atmos. Sci.*, *47*(21), 2580–2593.
- Pollack, J. B., C. B. Leovy, P. W. Greiman, and Y. Mintz (1981), A Martian general-circulation experiment with large topography, *J. Atmos. Sci.*, *38*(1), 3–29.

- Pollack, J. B., R. M. Haberle, J. Schaeffer, and H. Lee (1990), Simulations of the general circulation of the Martian atmosphere: 1. Polar processes, *J. Geophys. Res.*, *95*(B2), 1447–1473.
- Pollack, J. B., R. M. Haberle, J. R. Murphy, J. Schaeffer, and H. Lee (1993), Simulations of the general circulation of the Martian atmosphere: 2. Seasonal pressure variations, *J. Geophys. Res.*, *98*(E2), 3149–3181.
- Rafkin, S. C. R., R. M. Haberle, and T. I. Michaels (2001), The Mars regional atmospheric modeling system: Model description and selected simulations, *Icarus*, *151*(2), 228–256.
- Rannou, P., F. Hourdin, C. P. McKay, and D. Luz (2004), A coupled dynamics-microphysics model of Titan's atmosphere, *Icarus*, *170*(2), 443–462.
- Richardson, M. I., and R. J. Wilson (2002), Investigation of the nature and stability of the Martian seasonal water cycle with a general circulation model, *J. Geophys. Res.*, *107*(E5), 5031, doi:10.1029/2001JE001536.
- Rossow, W. B., and G. P. Williams (1979), Large-scale motion in the Venus stratosphere, *J. Atmos. Sci.*, *36*(3), 377–389.
- Schneider, E. K., and R. S. Lindzen (1977), Axially symmetric steady-state models of the basic state for instability and climate studies. Part I. Linearized calculations, *J. Atmos. Sci.*, *34*, 263–279.
- Skamarock, W. C., J. B. Klemp, J. Dudhia, D. O. Gill, D. M. Barker, W. Wang, and J. G. Powers (2005), A description of the Advanced Research WRF Version 2, *NCAR Tech. Note 468+STR*, Natl. Cent. for Atmos. Res., Boulder, Colo.
- Smagorinsky, J. (1963), General circulation experiments with the primitive equations, *Mon. Weather Rev.*, *91*(3), 99–164.
- Smith, M. D., J. C. Pearl, B. J. Conrath, and P. R. Christensen (2001), Thermal Emission Spectrometer results: Mars atmospheric thermal structure and aerosol distribution, *J. Geophys. Res.*, *106*(E10), 23,929–23,945.
- Smith, M. D., et al. (2004), First atmospheric science results from the Mars exploration rovers Mini-TES, *Science*, *306*(5702), 1750–1753.
- Stevens, B., and D. H. Lenschow (2001), Observations, experiments, and large eddy simulation, *Bull. Am. Meteorol. Soc.*, *82*(2), 283–294.
- Suarez, M. J., and L. L. Takacs (1995), Technical report series on global modeling and data assimilation, vol. 5, Documentation of the ARIES/GEOS dynamical core, version 2, *NASA Tech. Memo., NASA-TM 104606, REPT-95B00069-VOL-5, NAS 1.15:104606-VOL-5, 19950401*, NASA Cent. for Aerospace Inf. (CASI), Linthicum Heights, Md.
- Takahashi, Y. O., H. Fujiwara, H. Fukunishi, M. Odaka, Y. Hayashi, and S. Watanabe (2003), Topographically induced north-south asymmetry of the meridional circulation in the Martian atmosphere, *J. Geophys. Res.*, *108*(E3), 5018, doi:10.1029/2001JE001638.
- Taylor, F. W., D. M. Hunten, and L. V. Ksanfomaliti (1983), The thermal balance of the middle and upper atmosphere of Venus, in *Venus*, edited by D. M. Hunten et al., pp. 650–680, Univ. of Ariz. Press, Tucson.
- Toigo, A. D., and M. I. Richardson (2002), A mesoscale model for the Martian atmosphere, *J. Geophys. Res.*, *107*(E7), 5049, doi:10.1029/2000JE001489.
- Toigo, A. D., and M. I. Richardson (2003), Meteorology of proposed Mars Exploration Rover landing sites, *J. Geophys. Res.*, *108*(E12), 8092, doi:10.1029/2003JE002064.
- Toigo, A. D., M. I. Richardson, S. P. Ewald, and P. J. Gierasch (2003), Numerical simulation of Martian dust devils, *J. Geophys. Res.*, *108*(E6), 5047, doi:10.1029/2002JE002002.
- Tokano, T. (2005), Meteorological assessment of the surface temperatures on Titan: Constraints on the surface type, *Icarus*, *173*(1), 222–242.
- Tokano, T., and F. M. Neubauer (2002), Tidal winds on Titan caused by Saturn, *Icarus*, *158*(2), 499–515.
- Tokano, T., F. M. Neubauer, M. Laube, and C. P. McKay (1999), Seasonal variation of Titan's atmospheric structure simulated by a general circulation model, *Planet. Space Sci.*, *47*(3–4), 493–520.
- Toon, O. B., C. P. McKay, T. P. Ackerman, and K. Santhanam (1989), Rapid calculations of radiative heating rates and photodissociation rates in inhomogeneous multiple-scattering atmospheres, *J. Geophys. Res.*, *94*(D13), 16,287–16,301.
- Troen, I., and L. A. Mahrt (1986), A simple-model of the atmospheric boundary-layer-sensitivity to surface evaporation, *Boundary Layer Meteorol.*, *37*(1–2), 129–148.
- Tyler, D., Jr., J. R. Barnes, and R. M. Haberle (2002), Simulation of surface meteorology at the Pathfinder and VL1 sites using a Mars mesoscale model, *J. Geophys. Res.*, *107*(E4), 5018, doi:10.1029/2001JE001618.
- Wicker, L. J., and W. C. Skamarock (2002), Time-splitting methods for elastic models using forward time schemes, *Mon. Weather Rev.*, *130*(8), 2088–2097.
- Wilson, R. J., and K. Hamilton (1996), Comprehensive model simulation of thermal tides in the Martian atmosphere, *J. Atmos. Sci.*, *53*(9), 1290–1326.
- Wilson, R. J., Y. Takahashi, F. Forget, M. Mischna, T. Kuroda, Y. Moudden, and A. Medvedev (2006), Mars General Circulation Model intercomparison, paper presented at Second Mars Atmosphere Modelling and Observations Workshop, Cent. Natl. d'Etudes Spatiales, Granada, Spain. (Available at http://www.gfdl.noaa.gov/~rjw/MGCM_comparison/granada_2006_mgcm_comparison.ppt)
- Yamamoto, M., and M. Takahashi (2003a), The fully developed superrotation simulated by a general circulation model of a Venus-like atmosphere, *J. Atmos. Sci.*, *60*(3), 561–574.
- Yamamoto, M., and M. Takahashi (2003b), Superrotation and equatorial waves in a T21 Venus-like AGCM, *Geophys. Res. Lett.*, *30*(9), 1449, doi:10.1029/2003GL016924.
- Yamamoto, M., and M. Takahashi (2004), Dynamics of Venus' superrotation: The eddy momentum transport processes newly found in a GCM, *Geophys. Res. Lett.*, *31*, L09701, doi:10.1029/2004GL019518.
- Yamazaki, Y. H., D. R. Skeet, and P. L. Read (2004), A new general circulation model of Jupiter's atmosphere based on the UKMO Unified Model: Three-dimensional evolution of isolated vortices and zonal jets in mid-latitudes, *Planet. Space Sci.*, *52*(5–6), 423–445.
- Zurek, R. W., J. R. Barnes, R. M. Haberle, J. B. Pollack, J. E. Tillman, and C. B. Leovy (1992), Dynamics of the atmosphere of Mars, in *Mars*, edited H. H. Kieffer et al., chap. 26, pp. 835–933, Univ. of Ariz. Press, Tucson.

C. E. Newman and M. I. Richardson, Division of Geological and Planetary Sciences, California Institute of Technology, 1200 E. California Boulevard, MS 150-21, Pasadena, CA 91125, USA. (claire@gps.caltech.edu)

A. D. Toigo, Department of Astronomy, Cornell University, 326 Space Sciences Building, Ithaca, NY 14853, USA.